The Recombination of Propargyl Radicals and Other Reactions on a C_6H_6 Potential

James A. Miller* and Stephen J. Klippenstein*

Combustion Research Facility, Sandia National Laboratories, Livermore, California 94551-0969

Received: March 31, 2003; In Final Form: June 30, 2003

Using a combination of electronic-structure methods, we have explored in some detail the regions of the C_6H_6 potential that are important for describing the recombination of propargyl (C_3H_3) radicals. Using this information in an RRKM-based master equation, we have been able to predict rate coefficients for a variety of elementary reactions, including the $C_3H_3 + C_3H_3$ recombination itself. Generally, the agreement between the theory and the limited amount of experimental information available is very good, although some discrepancies remain. The most important new feature of the present analysis (over our previous one) is the inclusion of a path on the potential that connects 1,2,4,5-hexatetraene to 1,3-hexadien-5-yne and then goes on to benzene and phenyl + H without passing through fulvene. The inclusion of this path in the analysis allows a number of experimental observations to be accounted for by the theory. From the results of the master equation calculations, we propose a simple, contracted model for describing the rate coefficient and product distribution of the $C_3H_3 + C_3H_3$ recombination reaction (and subsequent isomerizations) for use in flame modeling. Modified Arrhenius expressions are provided for the rate coefficients of the reactions appearing in the simplified model.

I. Introduction

The recombination of propargyl radicals (C_3H_3) is a pivotal reaction in our understanding of the formation of aromatic compounds, polycyclic aromatic compounds (PAH), and soot in the combustion of alphatic fuels. Not only is the $C_3H_3 + C_3H_3$ reaction itself believed to be an important cyclization step in flames,[1−7] but it is also typical of other reactions that are likely to play an important role in the hydrocarbon growth process. The vast majority of such reactions take place over multiple, interconnected, potential wells, into any of which a C_6H_6 complex (in the present case) may be stabilized by collisions. Alternatively, such complexes may decompose to form one or more sets of bimolecular products. The fate of the reactants thus depends sensitively on the temperature, pressure, and perhaps the local composition. The theoretical analysis of the kinetics of such reactions is complicated even if one has a reliable potential energy surface in hand, requiring the solution of a time-dependent, multiple-well master equation (ME). Moreover, even if one is able to obtain such solutions, decomposing them into phenomenological rate coefficients that can be used in flame modeling is problematic, and only recently have systematic procedures been outlined for performing such a decomposition.[8,9] The present article addresses these issues for the propargyl recombination.

In a previous article[10] we studied the $C_3H_3 + C_3H_3$ reaction on the BAC-MP4 potential of Miller and Melius.[3,11] However, during the course of that work (and following it), it became clear to us that the Miller−Melius potential had some serious deficiencies. Among other things, comparison of our predictions with the experiments of Stein et al.[12] on 1,5-hexadiyne pyrolysis and Alkemade and Homann[13] on propargyl recombination clearly indicated that an important reaction path was missing, one that would link the early wells along the reaction path to 1,3-hexadien-5-yne and also provide a route to benzene that does not go through fulvene. These points are discussed in detail below. Subsequently, we found such a path, the crucial feature of which is a saddlepoint that connects 1,2,4,5-hexatetraene directly to 1,3-hexadien-5-yne. In the present article, using a combination of QCISD(T) and density functional methods we describe a completely new characterization of the features of the C_6H_6 potential that are important in propargyl recombination, including this new path. The resulting master equation model contains 12 potential wells and the associated transition states that connect them.

In addition to the $C_3H_3 + C_3H_3$ recombination, we discuss several isomerization processes that take place on the same potential. Some of these are included as a test of the accuracy of the potential, and some are necessary for a complete description of the propargyl recombination process itself.

II. Quantum Chemistry

Method. *Stationary Points.* The geometric structures and vibrational frequencies for all stationary points considered here were obtained via density functional theory employing the Becke-3−Lee−Yang−Parr (B3LYP) functional[14] and the 6-311++G(d,p) basis set.[15] The connections of each saddlepoint to its adjacent local minima were generally estimated through visualization of the corresponding imaginary vibrational mode. For a few uncertain cases intrinsic reaction coordinate calculations were also performed.

Higher level energies were obtained by two separate methods. Both methods employ a combination of quadratic configuration interaction calculations with perturbative inclusion of the triples contribution, QCISD(T),[16] and second-order Møller−Plesset perturbation theory (MP2).[15]

For the first method, HL1, the 6-311G(d,p) basis set is employed for the QCISD(T) calculations, and the 6-311++G-(3df,2pd) basis set is employed for the MP2 calculations. Also, the core electrons are treated as active in the MP2 evaluations for the latter basis set. Approximate QCISD(T,Full)/6-311++G-(3df,2pd) estimates, E_{HL1}, are then obtained as

10.1021/jp030375h CCC: $25.00
Published on Web 09/04/2003

$$E_{HL1} = E[\text{QCISD(T)/6-311G(d,p)}] + E[\text{MP2(Full)/6-311++G(3df,2pd)}] - E[\text{MP2/6-311G(d,p)}] \quad (1)$$

For the second method, we estimate the infinite basis set limit through the extrapolation of results obtained for sequences of the correlation-consistent, polarized-valence basis sets. The extrapolation is obtained from the expression[17,18]

$$E(\infty) = E(l_{max}) - B/(l_{max} + 1)^4 \quad (2)$$

where l_{max} is the maximum angular momentum in the basis set. The QCISD(T) extrapolation is obtained on the basis of calculations with Dunning's correlation-consistent, polarized-valence double-ζ (cc-pvdz) and triple-ζ (cc-pvtz) basis sets,[19] with $l_{max} = 2$ and 3, respectively. An MP2 calculation with the correlation-consistent, polarized-valence, quadruple-ζ basis (cc-pvqz) ($l_{max} = 4$) allows for two separate MP2 extrapolations: one from the cc-pvdz, cc-pvtz pair and one from the cc-pvtz, cc-pvqz pair. The final higher level estimate, E_{HL2}, is obtained as the sum of the QCISD(T) extrapolation and the difference between the two MP2 extrapolations. This combination of extrapolations can be expressed as

$$E_{HL2} = E[\text{QCISD(T)/cc-pvtz}] + \{E[\text{QCISD(T)/cc-pvtz}] - E[\text{QCISD(T)/cc-pvdz}]\}0.46286$$
$$E[\text{MP2/cc-pvqz}] + \{E[\text{MP2/cc-pvqz}] - E[\text{MP2/cc-pvtz}]\}0.69377$$
$$E[\text{MP2/cc-pvtz}] - \{E[\text{MP2/cc-pvtz}] - E[\text{MP2/cc-pvdz}]\}0.46286 \quad (3)$$

Zero-point energy corrections are evaluated at the B3LYP/6-311++G(d,p) level and are incorporated in the final energies reported below. The Gaussian-98 quantum chemistry software was employed in all the electronic-structure calculations described here.[20]

Heats of formation were obtained from calculations of the heat of reaction for decomposition into H_2 and CH_4, coupled with experimental values for the heats of formation of H_2 and CH_4. The use of such molecular (i.e., CH_4 and H_2), rather than atomic, references ameliorates a number of errors, such as those due to anharmonic effects, spin−orbit effects, etc. Extensive comparison with experimental heats of formation for a wide range of pure hydrocarbons indicates that both HL1 and HL2 predictions are highly accurate, rarely differing by more than 1.0 kcal/mol from experiment, typically being within a few tenths of a kcal/mol.[21] In general, one might expect the HL2 results to be more accurate than the HL1 ones. However, the HL2 calculations were not finished until after the completion of the kinetic analysis, and so the kinetic analysis was performed using the HL1 energies, which are not much different from the HL2 values anyway.

Spin-restricted wave functions were generally employed in both the B3LYP and Hartree−Fock evaluations. However, for the H-loss transition states from wells IX, X, and XI, and for the cis−trans isomerization from well VIII to XII, spin-restricted wave functions were unsuitable, and so unrestricted wave functions were employed instead. The calculated "averaged-spin-squared" for these four transition states was, respectively, 1.01, 1.04, 1.01, and 1.06 at the B3LYP/6-311++G** level and 1.45, 1.71, 1.46, and 1.45 at the HF/6-311G** level. The strong spin contamination in these states correlates with significantly increased uncertainty in the corresponding energy estimates.

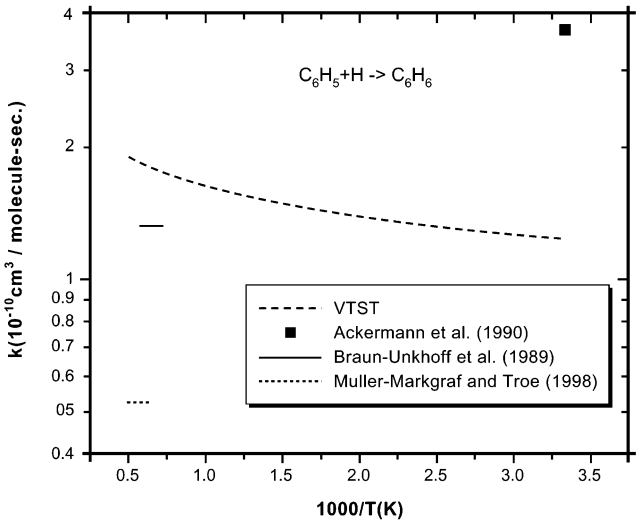

Figure 1. High-pressure-limit rate coefficient for H + phenyl → benzene.

Potential Energy Surfaces for the Barrierless Channels. The variable reaction coordinate transition state theory[22,23] analysis employed here for the barrierless reactions to form channels I, II, and V from reactants and to produce H + phenyl from benzene requires analytic potential energy surfaces for the interaction between the two fragments. For the three entrance channels, the analytic model potentials described in our previous study,[10] which involved a fit to estimated high-pressure rate coefficients, were again employed. For the H + phenyl channel, an a priori potential, based on the close analogy between this reaction and the H + vinyl reaction, was employed. A high-quality ab initio potential for the latter reaction was presented in ref 24. This potential was obtained from fits to wide-ranging CAS+1+2/cc-pvdz calculations coupled with CAS+1+2/cc-pvtz basis set corrections along the minimum energy path. Assuming that the interactions of the H atom with the phenyl group are identical to those calculated for the interaction between the H atom and the vinyl group (for the CH_2 end of the front side addition channel) yields the calculated high-pressure addition rate coefficients plotted in Figure 1. Although the theoretical predictions are not in agreement with any of the experimental values,[25−27] they do provide a reasonable representation of the "average" experimental result. These values are about a factor of 2 larger than those predicted by Mebel et al. on the basis of B3LYP/6-311G** ab initio calculations and rigid-rotor, harmonic-oscillator based canonical variational transition-state theory.[28] The present theoretical predictions for the high-pressure-limit H + phenyl addition rate coefficient are well represented by the expression, 1.24×10^{-10} $(T/298)^{0.228}$ $\exp(-5.05/T)$ cm^3 s^{-1} $molecule^{-1}$, over the 300−2000 K temperature range.

Results. The present determination of the potential energy surface for the $C_3H_3 + C_3H_3$ system builds on the pioneering BAC-MP4 studies of Melius and his collaborators.[3,11] In subsequent studies, Mebel and co-workers provided higher level G2M estimates for many of the same stationary points investigated by Melius et al. and, in addition, they explored a number of other features of the surface.[28−30] Schaefer and co-workers have provided a detailed analysis of the ring topomerization pathways, including an extensive treatment of a number of paths relevant to the fulvene → benzene isomerization.[31] Taken together, these investigations provide a reasonably complete description of the low-energy isomerization and decomposition pathways. However, no single study has considered all aspects

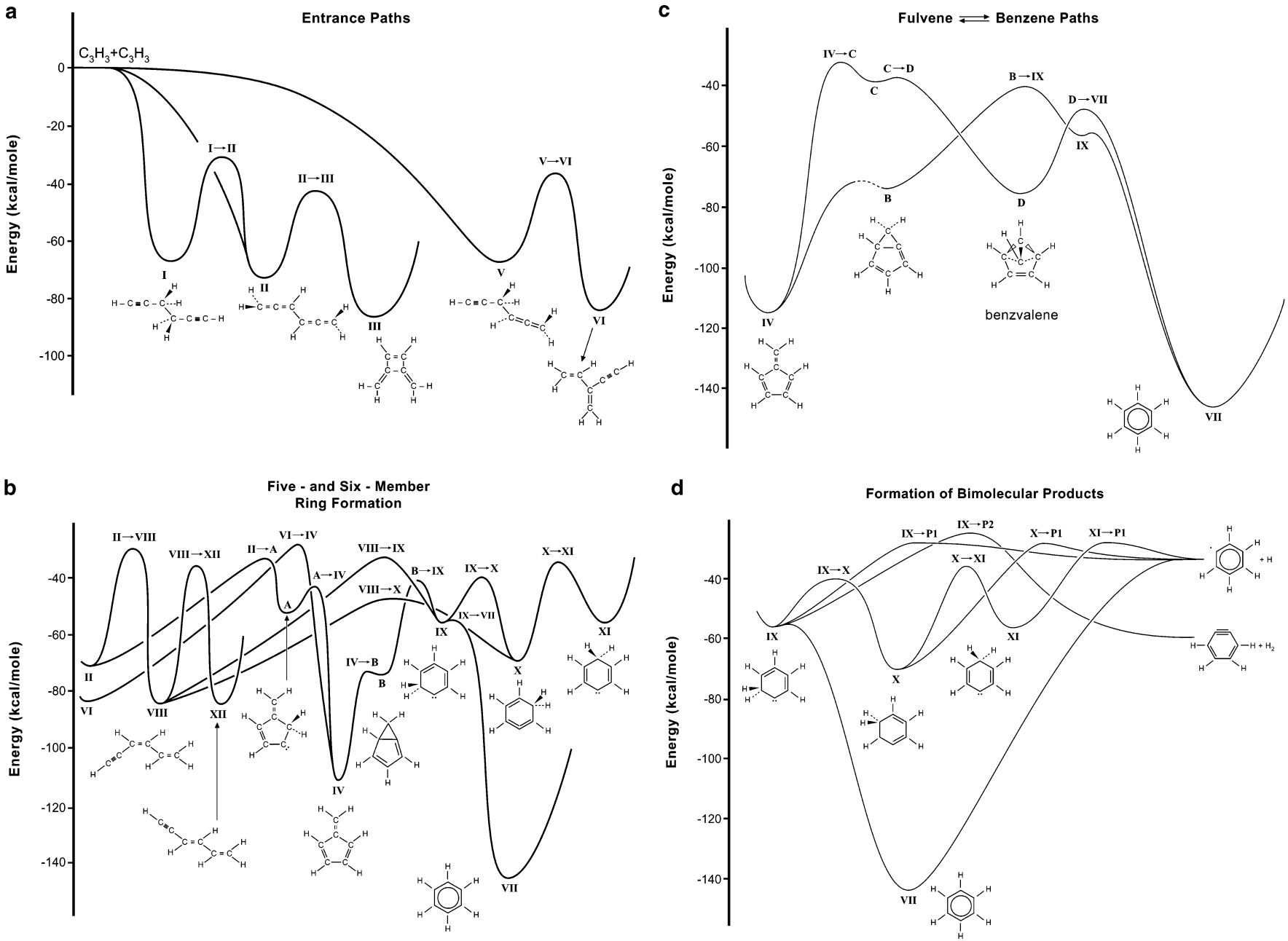

Figure 2. Reaction path diagram for the C_6H_6 potential used in the present analysis.

TABLE 1: Heats of Formation for the $C_3H_3 + C_3H_3$ System (0 K)[a]

species	HL1	HL2	BAC-MP4[b]	G2M
Reactants				
$CH_2CCH+CH_2CCH$; (R)	169.8	169.4	167.2	
Wells				
$CHCCH_2CH_2CCH$; (I)	102.7	102.1	106.2	
$CH_2CCHCHCCH_2$; (II)	97.2	97.5	99.4	98.4[d]
$-C(CH_2)CHCHC(CH_2)-$; (III)	83.6	83.9	83.5	
$-CHCHC(CH_2)CHCH-$; (IV)	54.7	54.6	56.2	53.6[d]
$CHCCH_2CHCCH_2$; (V)	102.4	102.5	107.2	
$CH_2CHC(CH_2)CCH$; (VI)	85.8	85.8	85.4	
$-CHCHCHCHCH-$; (VII)	24.2	23.4	21.3	23.4
$CHCCHCHCH_2$; (VIII) cis,trans	85.0	84.8	82.9	
$-CCH_2CHCHCH-$; (IX)	113.6	112.9	117.7	112.2[c]
$-CCHCH_2CHCH-$; (X)	98.8	99.0	94.6	100.7[c]
$-CCHCHCH_2CHCH-$; (XI)	114.2	113.7		116.3[c]
$CHCCHCHCHCH_2$; (XII) trans,trans	85.0	84.8	83.3	83.9[c]
Saddlepoints				
I → II	138.1	137.7	134.1	
II → III	126.8	127.5	121.9	
II → A	136.3	136.9	131.8	134.7[d]
A → IV	126.2	126.1	130.0	125.1[d]
II → VIII	138.9	139.5		137.7[d]
IV → VI	141.4	141.4	144.2	
IV → C	137.4	137.0	136.6	137.8[e]
C → D	131.2	132.7		132.6[e]
D → VII	122.6	123.9		121.7[e]
B → IX	129.0	128.8	129.3	128.1[e]
V → VI	132.4	133.6	140.1	
VII → IX	113.6	113.0	116.3	112.8[c]
VIII → IX	136.6	136.5		134.1[c]
VIII → X	122.6	122.8	113.9	124.0[c]
VIII → XII	134.1		128.0	
IX → X	129.8	129.2		132.0[c]
IX → P_1	142.9			144.8[c]
IX → P_2	145.9	145.0		144.8[c]
X → XI	135.2	134.7		137.5[c]
X → P_1	142.8			144.8[c]
XI → P_1	143.1			145.0[c]
Products				
$C_6H_5 + H$ (P_1)	137.0	137.1	134.2	138.6[c]
o-$C_6H_4+H_2$ (P_2)	111.3	111.3	103.6	109.5[c]
Intermediates				
A; between II and IV	117.2	116.8	117.8	115.8[d]
C; between IV and VII; a	131.6	131.8	134.6	130.9[e]
D; between IV and VII; b	94.1	95.7	98.8	94.5[e]
B; between IV and IX	95.9	96.6	93.8	95.1[e]

[a] All energies in kcal/mol. [b] BAC-MP4 enthalpies from ref 11. [c] G2M enthalpies from ref 29. [d] G2M enthalpies from ref 28. [e] G2M enthalpies from ref 30.

of the potential required to treat the thermal kinetics of propargyl recombination. In the interest of developing a consistent, high-level model, we have undertaken a reanalysis of all the stationary points pertinent to the thermal isomerization/dissociation kinetics, employing the same high-level ab initio methodologies throughout. For completeness, and to motivate the kinetic analysis, the overall potential energy surface is reviewed briefly.

A schematic diagram of the potential energy surface obtained on the basis of the present HL1 calculations is provided in Figure 2. The corresponding stationary point structures are illustrated in Figure 3. The Cartesian coordinates and vibrational frequencies of these points are available as Supporting Information. Figure 2a illustrates the three different wells (I, II, and V) that can be accessed via simple addition of the two radicals. Also shown therein are two more wells (III, VI) that are accessible via comparatively low-lying saddlepoints. Note that the pathway from V to VI actually involves an intermediate that also plays a role in the production of fulvene (IV) from V and/or VI.[3,11] Here we ignore that intermediate in the kinetic analysis, as discussed in our previous study of this reaction.[10]

Figure 2b illustrates the low-energy pathways from these initial wells that lead to fulvene and/or benzene. This aspect of the potential energy surface differs significantly from that of the earlier BAC-MP4 studies in the inclusion of a path from well II to well VIII. Benzene (VII) can be produced from well VIII via ring closure to form wells IX or X followed by H transfers. Importantly, this pathway provides a parallel route from well II to benzene that does not pass through fulvene, and which has a similar peak barrier energy. At higher energies this path provides the dominant route to benzene formation. The pathway from II to VIII was also discussed by Mebel and co-workers in examining the production of $C_5H_3 + CH_3$ from benzene.[28] However, its importance to the $C_3H_3 + C_3H_3$ reaction has not previously been recognized. In Figure 2b, well XI arises from an H transfer in well X, whereas well XII results from a cis−trans isomerization about the central CC double bond in well VIII.

In previous studies, the formation of benzene was presumed to arise only from the isomerization of II to IV, via the intermediate A, followed by the isomerization of IV to IX via the intermediate B. An alternative IV → VII pathway, proceeding through two separate intermediates (C and D), has also been considered in the present analysis. The latter pathway is illustrated in Figure 2c, together with the related IV → B → VII pathway. Both pathways are explicitly included in the kinetic analysis.

The pathways for bimolecular product formation, phenyl + H (P_1) or *o*-benzyne + H_2 (P_2), are illustrated in Figure 2d. The formation of $C_6H_5 + H$ should be the dominant bimolecular pathway, because the reverse association is barrierless and the transition state is low in energy. Although pathways to produce *m*- and *p*-benzyne should exist, it is unlikely that their transition states lie lower than that for formation of *o*-benzyne. Thus, such pathways have not been considered here.

The numerical values for the present HL1 and HL2 calculations of the stationary point 0 K heats of formation are presented in Table 1, together with prior BAC-MP4 and G2M results. In tabulating the latter numbers we have used benzene as a reference, because the investigators involved report only relative energies. The HL1 and HL2 results in Table 1 are remarkably similar, with only 3 pairs of energies differing by more than 0.8 kcal/mol, and even the largest of these differs by only 1.5 kcal/mol. The kinetic analysis presented below employs the HL1 energies. Very similar results would be obtained with the HL2 energies. In contrast, the BAC-MP4 results commonly differ from the HL1 energies by 4−5 kcal/mol; such a disparity results in significant differences in the kinetic predictions. Meanwhile, the HL1 and G2M predictions are in fairly reasonable agreement, with typical differences of 1−2 kcal/mol.

III. Determining Phenomenological Rate Coefficients from Solutions to the Master Equation

We have discussed previously our methods for handling hindered rotations, calculating sums and densities of states, and obtaining microcanonical (and microcanonical/J-resolved) RRKM rate coefficients from properties of the potential energy surface.[32] We have also discussed several times the formulation of the multiple-well master equation.[33−36] It seems unnecessary to repeat those discussions here. Rather, in the following paragraphs we briefly review the methods we have developed for obtaining phenomenological rate coefficients from solutions to the master equation.[8,9] In the present work, unlike our previous

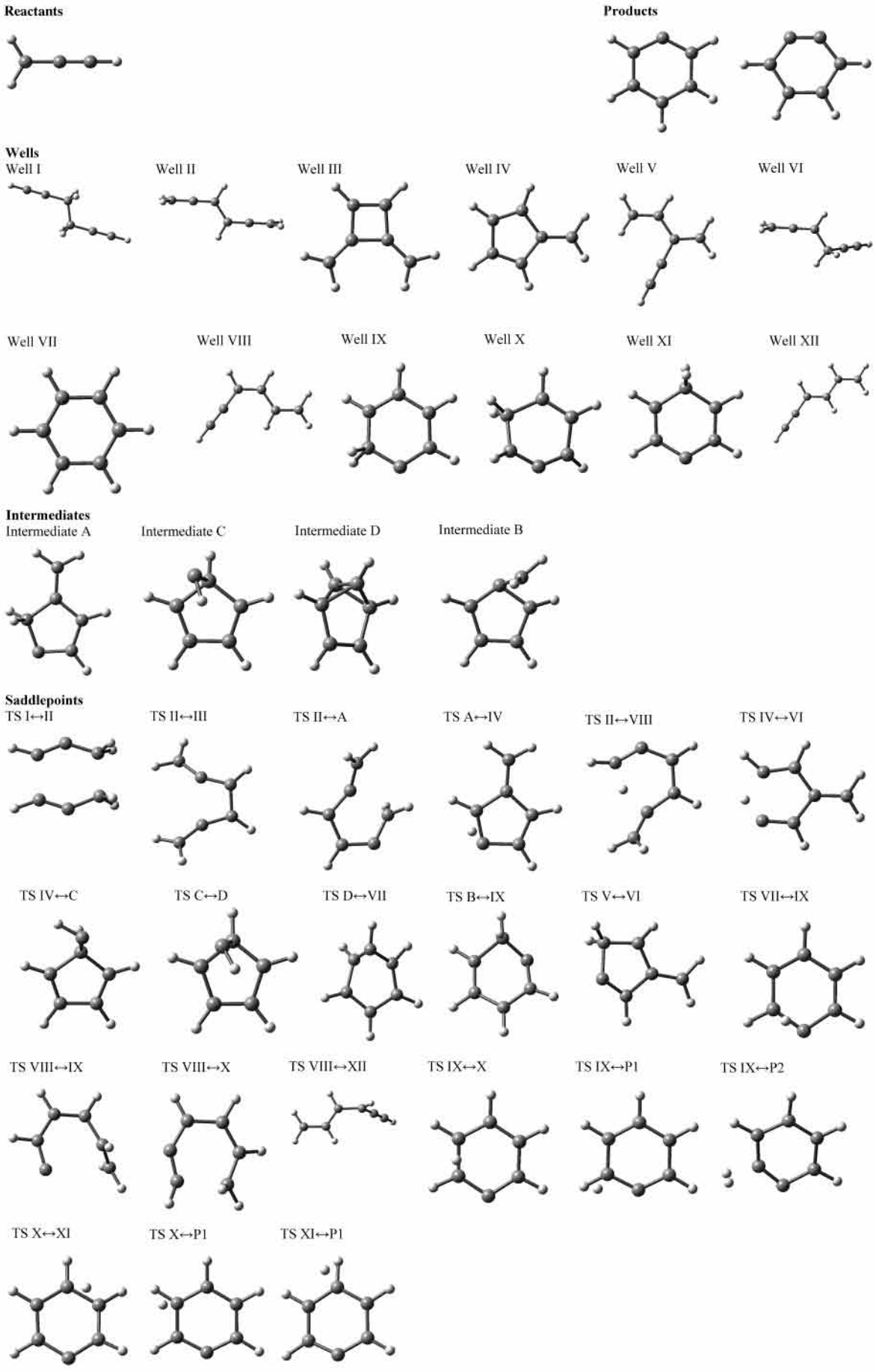

Figure 3. Structure of the stationary points of the C_6H_6 potential depicted in Figure 2.

analysis of the $C_3H_3 + C_3H_3$ reaction,[10] we include tunneling one-dimensionally through the tight transition states by assuming that the reaction path can be described by an Eckart function.

As in our previous article on propargyl recombination,[10] we consider a situation in which the reactants are highly dilute in a bath of nitrogen (N_2). Moreover, to make the master equation linear, we envision two types of propargyl radicals, one whose concentration greatly exceeds that of the other, i.e.

$$n_{N_2} \gg n_m \gg n_R \tag{4}$$

where n_{N_2}, n_m, and n_R are the number densities of N_2, the "excess" propargyl radicals, and the "deficient" propargyl radicals, respectively. If two of the "excess" propargyls react with each other, we remove the products from our system and replace the reactants immediately. In this way n_m = constant, and our master equation is linear. Although it is inadequate to simulate any real experiment, such a model does yield correct values for phenomenological rate coefficients, which is the desired result.

Under the conditions described in the previous paragraph, the master equation, which is one-dimensional in the total internal energy E, can be expressed in the simple form[2,10,33−36]

$$\frac{d|\mathbf{w}\rangle}{dt} = \mathbf{G}|\mathbf{w}\rangle \tag{5}$$

where $|\mathbf{w}\rangle$ is a vector whose components contain the relevant state populations, and $\boldsymbol{G}$ is a real, symmetric matrix. The solution to eq 5 can be written concisely as

$$|\mathbf{w}(t)\rangle = \hat{T}|\mathbf{w}(0)\rangle \tag{6}$$

where $|\mathbf{w}(0)\rangle$ is the initial-condition vector, and $\hat{T}$ is the time-evolution operator,

$$\hat{T} = \sum_{j=0}^{N} e^{\lambda_j t}|g_j\rangle\langle g_j| \tag{7}$$

The vectors $|g_j\rangle$ and the scalars λ_j satisfy the eigenvalue equation

$$\mathbf{G}|g_j\rangle = \lambda_j|g_j\rangle \qquad j = 0, ..., N \tag{8}$$

The solution to the master equation thus reduces to diagonalizing **G**. A particularly useful property of this solution is that, once **G** has been diagonalized at any pressure and temperature (p and T), the resulting $\hat{T}$ matrix can be used to operate on any initial condition vector and determine the time evolution of the system.

In a typical application N is in the thousands. However, these "normal modes of relaxation" (the eigenpairs of **G**) separate neatly into two types under ordinary conditions. Those with the smallest eigenvalues (the most negative) describe the relaxation of the internal energy of the isomers under consideration. We call these modes IERE's (internal energy relaxation eigenpairs or eigenvalues). The IERE's relax very rapidly, and their eigenvalues are so closely spaced that they essentially form a continuum. The remainder of the relaxation modes describe chemical change. Generally, their eigenvalues are algebraically much larger (less negative) than the IERE's, and consequently they relax much more slowly. It is only under such conditions, i.e., with such a separation of time scales, that we can expect a phenomenological description of the chemistry to apply.[8,9,37−40] We call these slow relaxation modes CSE's (chemically significant eigenpairs or eigenvalues). The vast majority of the relaxation modes are IERE's. If there are S "species", or chemical configurations, in a problem, there are only

$$N_{chem} = S - 1 \tag{9}$$

CSE's[2,8,9] in addition to $\lambda_0 = 0$ and $|g_0\rangle$, which themselves describe a state of complete thermal and chemical equilibrium. Of course all the eigenvalues except λ_0 are negative; otherwise the solution given by eqs 6 and 7 would blow up as $t \to \infty$, rather than approach equilibrium. We assign the subscript 1 to the largest (least negative) of these $S - 1$ negative eigenvalues, 2 to the next largest, etc.; $|g_1\rangle$, $|g_2\rangle$, ... are the corresponding eigenvectors. At the same time, for a problem with S species, there are

$$N_k = \frac{S(S-1)}{2} \tag{10}$$

forward rate coefficients and an equal number of reverse rate coefficients. Figure 2 shows that in our formulation of the propargyl recombination problem $S = 15$ ($C_3H_3 + C_3H_3$, phenyl + H, orthobenzyne + H_2, and 12 isomers of C_6H_6). Consequently, according to eq 10 N_k should be 105. However, because we have combined phenyl + H and orthobenzyne + H_2 into a single "infinite sink", one forward rate coefficient and one reverse rate coefficient are missing, i.e., those corresponding to the reaction phenyl + H $\rightleftarrows$ orthobenzyne + H_2. Therefore, N_k is actually equal to 104. This is still a large number of rate coefficients, but most of them are only of passing interest to us. It is this large number of isomerization and dissociation (to phenyl + H and orthobenzyne + H_2) rate coefficients that complicates the task of extracting the $C_3H_3 + C_3H_3$ product distribution from the raw time histories obtained from solutions to the ME.

In previous work,[8,9] we have derived two methods of obtaining phenomenological rate coefficients from the CSE's, including a general prescription for dealing with multiple infinite-sink products. Let us review those results briefly. The eigenpair-based solution of the master equation gives the species populations in the form

$$X_i(t) = \sum_{j=0}^{N_{chem}} a_{ij} e^{\lambda_j t} \qquad i = I, ..., M, R, P_1, P_2 \tag{11}$$

where M = XII (in the present case) is the number of wells, and $X_i(t)$ is the fraction of the initial reactant concentration (either the deficient reactant R or one of the C_6H_6 isomers) that is present in configuration i at time t. The bimolecular products P_1 and P_2 are, respectively, phenyl + H and orthobenzyne + H_2 in the problem at hand. The coefficient $a_{i0} = X_i(\infty)$ is nominally the equilibrium population of the i-th configuration, and $a_{ij} = -\Delta X_{ij} (j \neq 0)$, where ΔX_{ij} is the change in population of the i-th configuration that accompanies the time evolution of the j-th eigenpair from $t = 0$ to $t = \infty$. The ΔX_{ij}'s and the λ_j's, which are the fundamental quantities needed for calculating the rate coefficients, come from diagonalizing **G**. The assumption that P_1 and P_2 are infinite sinks introduces some minor complications, but these issues can be dealt with in a relatively straightforward manner.[9] Note that in the presence of 1 or more sinks, the system does not approach equilibrium as $t \to \infty$, but instead all the population goes to P_1 and P_2. The problem is to get the 104 phenomenological rate coefficients, $k(T,p)$, from the time evolution of the populations given by eq 11.

The problem of extracting the rate coefficients from the eigenvalues and eigenvectors of **G** can be approached in one of (at least) two different ways.[8,9] The first (and simplest) is to

use different inital-condition vectors in eq 6, differentiate the resulting species populations given by eq 11 with respect to time, and take the limit as $t \rightarrow 0$. One thus obtains the rate coefficients in the form

$$k_{\mathrm{Ti}} = \sum_{j=1}^{N_{\mathrm{chem}}} \lambda_j \Delta X_{ij}^{(\mathrm{i})}$$
$$k_{\mathrm{i}l} = -\sum_{j=1}^{N_{\mathrm{chem}}} \lambda_j \Delta X_{lj}^{(\mathrm{i})} \qquad (12)$$

where the superscript on $\Delta X_{ij}^{(\mathrm{i})}$ indicates that the reactant is species i. The rate coefficients k_{Ti} and k_{il} represent the total rate coefficient for removal of species i and the i $\rightarrow$ *l* rate coefficient, respectively.

The second method is more aesthetically pleasing, but more difficult to implement under some conditions. It utilizes a single (but arbitrary) initial condition and exploits the fact that eq 11 is the solution to a system of first-order rate equations with the rate coefficients,

$$k_{\mathrm{Ti}} = -\sum_{j=0}^{N_{\mathrm{chem}}} \lambda_j a_{\mathrm{i}j} b_{j\mathrm{i}}$$

and (13)

$$k_{\mathrm{i}l} = \sum_{j=0}^{N_{\mathrm{chem}}} \lambda_j a_{lj} b_{j\mathrm{i}}$$

If the a_{ij} are considered to be the elements of a matrix **A**, the b_{ij} in eq 13 are the elements of its inverse, $\mathbf{B} = \mathbf{A}^{-1}$. In both methods, if the reaction of interest is actually bimolecular, e.g., the $C_3H_3 + C_3H_3$ reaction itself, the rate coefficients given by eqs 12 and 13 are actually pseudo-first-order rate coefficients and must be divided by n_{m} to give the true bimolecular rate coefficients. Equations 12 and 13 virtually always give the same results. We tend to rely more heavily on the first method because of its computational simplicity.

Note that the upper limit on the sums in eqs 12 and 13 is $j = N_{\mathrm{chem}}$. This limit should serve to remind us of the fundamental assumption on which the analysis is based, i.e., the large separation of time scales between the CSE's and the IERE's. Such a separation of time scales is virtually always satisfied at room temperature and even for several hundred Kelvins above room temperature. However, as $T \rightarrow \infty$ the approach to equilibrium is not so orderly, and chemical and internal energy relaxation time scales become comparable in magnitude. Of course, combustion involves high temperatures, making it necessary to modify the approach outlined above to account for this transition from the "rate-coefficient regime" that exists at low *T* to the more chaotic situation that takes its place at very high temperatures.

Figure 4 shows three eigenvalue spectra (λ_j as a function of temperature), one for $p = 30$ Torr, one for $p = 1$ atm, and one for $p = 10$ atm. All these calculations were done with a value of the partial pressure of the excess reactant equal to 1 Torr. One can label the curves in Figure 4 in a number of different ways. One could label them simply by magnitude, as discussed above. We have done this in Figure 4 at low *T* and kept the same labeling at high *T* despite crossings of the curves. Alternatively, one could label them by transition state, as we have done in the past.[10,35] This method leads to considerable insight into the chemical processes occurring on the potential and results in avoided crossings of some curves caused by shifts

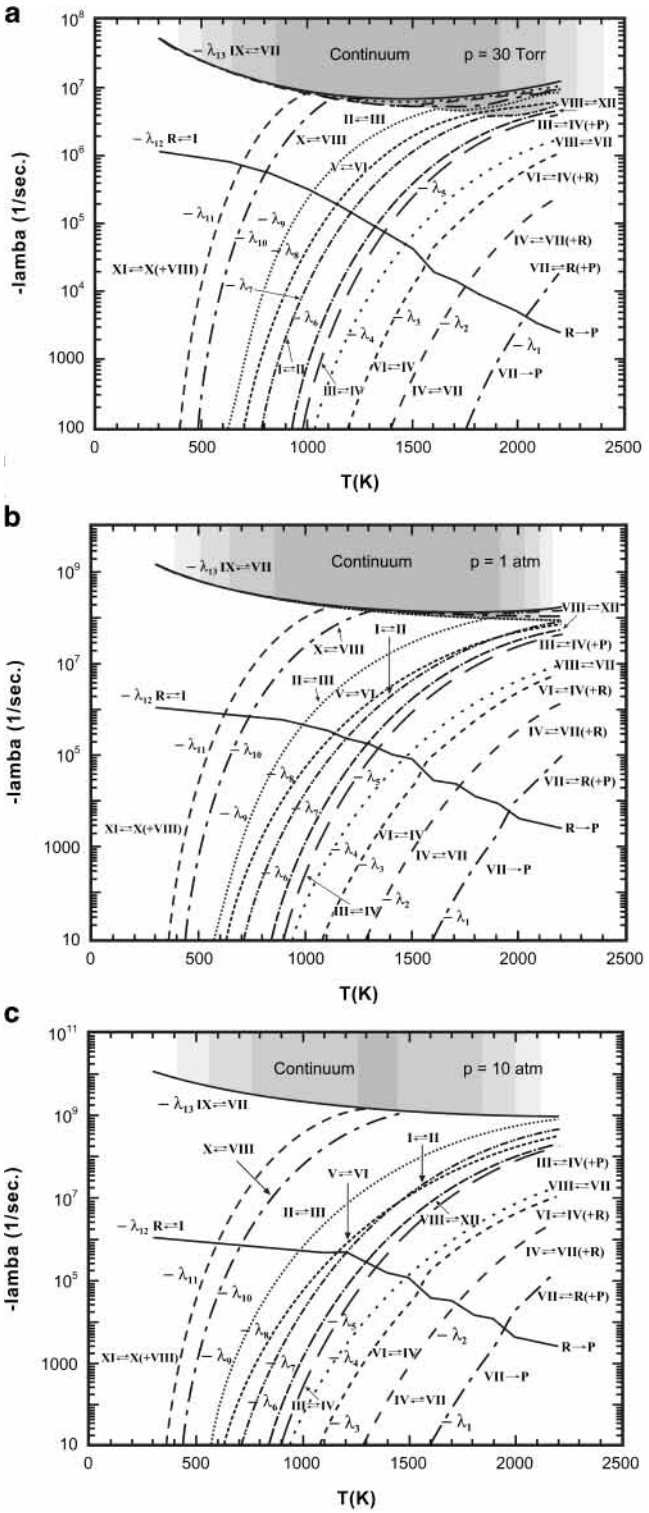

Figure 4. Eigenvalue spectrum of **G** as a function of temperature. Each curve is labeled by the chemical equilibrium that the corresponding eigenpair brings into being, as well as by magnitude of the eigenvalue at low temperature. Pressure: (a) $p = 30$ Torr; (b) $p = 1$ atm; (c) $p = 10$ atm.

in chemical equilibria.[10,35] A third method of labeling the eigenvalue curves is by the equilibration processes that the corresponding eigenpairs (i.e., the CSE's) bring about. Each chemically significant eigenpair describes the approach to the chemical equilibrium of two species (not necessarily through a single elementary reaction); more than two species may be involved if one or the other of the 2 has already come to equilibrium with one or more other species. Complete chemical

equilibrium in the rate-coefficient regime is thus reached through a sequence of well-defined steps. The curves in Figure 4 are labeled in this way, as well as by their low-T magnitude. For example, λ_{11} (and its eigenvector $|g_{11}\rangle$) equilibrate the process XI $\rightleftarrows$ X; the (+VIII) simply indicates that well VIII is also a major product. Then λ_{10} and $|g_{10}\rangle$ equilibrate well X (which was equilibrated on a faster time scale with XI) with well VIII, and so on. An interesting point to notice is that there appear to be only 12 CSE's in Figure 4, whereas there really should be 13. This occurs because the potential energy barrier that separates well IX from well VII is extremely small; the IX $\rightleftarrows$ VII equilibration process thus occurs on a time scale comparable to the IERE's, even at very low temperatures. Consequently, the corresponding eigenvalue is embedded in the continuum of IERE's in Figure 4.

The curve corresponding to λ_{12} is jagged at high temperature. This happens because of an interesting phenomenon that can occur when two equilibration processes have a species in common. Away from the crossing of such eigenvalue curves, each eigenpair has its distinct equilibration function, but near a crossing, the eigenvectors "mix" in that each can take on some of the character of the other. The two equilibration processes still take place, but not individually through separate eigenpairs. The jaggedness is a consequence of an unavoidable mislabeling in such circumstances. If we had labeled the curves by transition state, most (if not all) of the crossings that cause the jaggedness would likely turn out to be avoided crossings.[10,35]

As temperature increases, each of the eigenvalue curves in Figure 4 sequentially crosses into the continuum of IERE's, in principle violating the "separation-of-time scale" assumption that underpins a phenomenological description of the chemical kinetics. However, the rate-coefficient description can be extended by the following device. When an eigenvalue curve crosses into the continuum, it means that the associated chemical equilibration process takes place as fast as collisional energy transfer. For our purposes, the species involved cease to be "distinct". Therefore, we combine them! For kinetic purposes, the equilibrating thermodynamic species become part of a kinetic superspecies. Mathematically this means that we can reduce the number of terms in the sums of eqs 12 by one each time an eigenvalue is absorbed by the continuum. Also, the **A** and **B** matrices of eqs 13 are reduced by one row and one column at the same time. As a result, both methods continue to give a good, although contracted, phenomenological description of the chemical kinetics at high temperature. Failure to adopt this methodology ultimately results in nonsensical (frequently negative) rate coefficients at high T. The procedure, however, is quite forgiving in that it appears not to make too much difference whether one makes the system reduction at a temperature slightly before or coincident with the crossing of the eigenvalue into the continuum. From our experience, the species most affected by this choice are usually minor products of the reaction of interest.

As we have noted previously,[9] the rate-coefficient approximation is more robust at higher pressures. Collisional energy transfer rates are proportional to the pressure, whereas chemical reaction rates generally have a weaker pressure dependence. As a consequence, the temperature at which a CSE is absorbed by the continuum is higher at higher pressures. This can be seen clearly in Figure 4.

At low temperatures, because of their small magnitude, it can be difficult (if not impossible) to obtain accurate eigenvalues and eigenvectors of **G**. In the present investigation we have solved this problem by integrating the ME directly in time[10] using an ODE solver, resorting to the "exponential-decay" approach[10,33−36] to determine rate coefficients and product distributions. Under such conditions, the CSE's are generally well separated in magnitude, and problems that we have identified previously with this approach[8] can be avoided.

The vast majority of the ME solutions reported in this article are one-dimensional in E, the total internal energy. However, for the limiting case that $p \rightarrow 0$, we can also solve a two-dimensional ME with E and J, the total angular-momentum quantum number, the independent variables.[36,41] Both one- and two-dimensional solutions for the collisionless-limit ME were computed for this article.

In all the master equation calculations we use a single exponential-down model for the energy transfer function, $P_i(E,E')$, i = I, ..., M, with $\langle \Delta E_d \rangle$ independent of i. The values of $\langle \Delta E_d \rangle$ were chosen to have the temperature dependence

$$\langle \Delta E_d \rangle = 400\left(\frac{T}{300\ \mathrm{K}}\right)^{0.7}\ \mathrm{cm}^{-1} \qquad (14)$$

This model results in room-temperature values of $\langle \Delta E \rangle$ that are similar to those obtained experimentally for toluene[42] at the relevant energies. The temperature dependence is loosely based on our analysis of collisional energy transfer in CH_4 dissociation.[43] The collision rate Z is calculated from Lennard-Jones potentials. Note that $\langle \Delta E_d \rangle$ given by eq 14 is larger at high temperatures than the value $\langle \Delta E_d \rangle = 500\ \mathrm{cm}^{-1}$ used in our previous investigation of this reaction. However, this difference is only a secondary factor in the larger rate coefficients reported below. All calculations reported in this investigation, even those using the older potential, incorporate $\langle \Delta E_d \rangle$ from eq 14.

All the rate-coefficient calculations reported here were done with VARIFLEX.[44]

IV. Low-Temperature Isomerizations

The C_6H_6 potential embraces a large number of elementary reactions and rate coefficients, but surprisingly few of them have actually been studied in the laboratory. However, there have been several important experimental investigations of the isomerizations of the C_6H_6 isomers located early along the reaction path of Figure 2.[11,12,45−47] These experiments provide a good test of our theory, particularly of the accuracy and completeness of the potential. In making comparisons with these experiments we found it desirable to increase the I $\rightarrow$ II and II $\rightarrow$ III barrier heights by 1.0 and 0.71 kcal/mol, respectively, over those calculated by the HL1 method described above. Such changes are well within any accuracy limits we might assign to the calculations. No other PES properties were altered in the rate-coefficient calculations presented here.

The most important of these experiments for our purposes are those of Stein et al.[12] These experimenters studied the pyrolysis of 1,5-hexadiyne (well I) at 1 atm pressure in a flow reactor in the temperature range 523 K $\leq T \leq$ 823 K. They also studied the same reaction in very low-pressure pyrolysis experiments, but such experiments are dominated by wall collisions and consequently are not very useful to us directly. In the atmospheric-pressure experiments, product distributions were determined for a residence time of $\tau \approx 30$ s. Figure 5 compares our predictions of the product yield with their experiments as a function of temperature. For this comparison we integrated the ME directly in time, using the ODE method, to the specified time of 30 s. The agreement between theory and experiment is quite good. At the lower end of the temperature range the 1,5-hexadiyne is converted completely

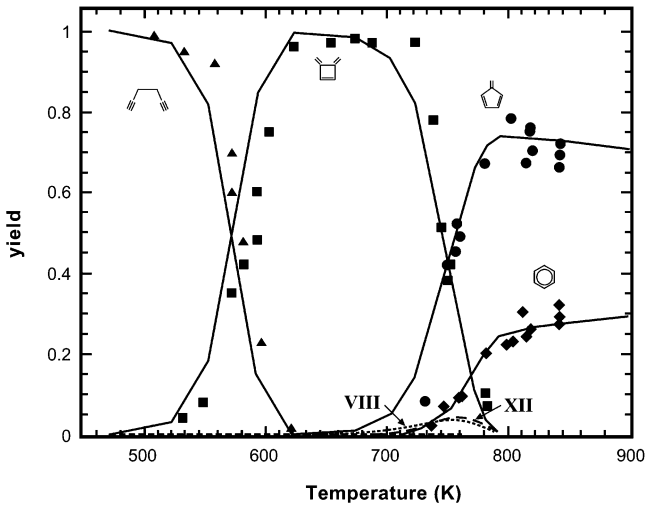

Figure 5. Product yields in the pyrolysis of 1,5-hexadiyne as a function of temperature at $p = 1$ atm. The residence time τ is equal to 30 s. The experimental data are from Stein et al.[12]

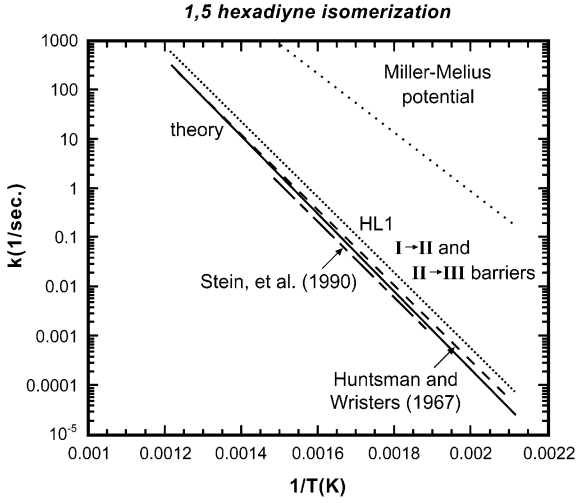

Figure 6. Arrhenius plot of the I → III rate coefficient.

to 1,2-dimethylenecyclobutene. No significant population accumulates in well II because of the small II−III potential energy barrier, even though well II lies directly in the path between I and III. At higher temperatures, benzene and fulvene are formed simultaneously as products of 1,2 dimethylenecyclobutene pyrolysis with a fulvene/benzene ratio of more than 2:1. The theory predicts this behavior quite well; it also shows some very small accumulation in wells VIII and XII between 700 and 800 K, apparently not detected in the experiments. The *simultaneous* formation of benzene and fulvene requires parallel paths to these species from well III, not a single path along which the two wells are located sequentially, as on the Miller−Melius potential.[3,11] This point is discussed in detail below.

From their data, Stein et al. determined a value of $10^{11.7}$ exp($-35500/RT$) s^{-1} [$R = 1.987$ cal/(mol K)] for the I → III rate coefficient between 523 and 673 K. We compare our predictions with their results in Figure 6. Also shown on the plot are the experimental result of Huntsman and Wristers,[45] our prediction of the rate coefficient with the unaltered HL1 potential barriers, and the same prediction with the Miller−Melius PES. Our best theoretical rate coefficient lies between the two experimental results, with the basic HL1 prediction lying roughly a factor of 2−3 higher. The Miller−Melius PES predicts a rate coefficient that is about 3 orders of magnitude too large, a consequence of

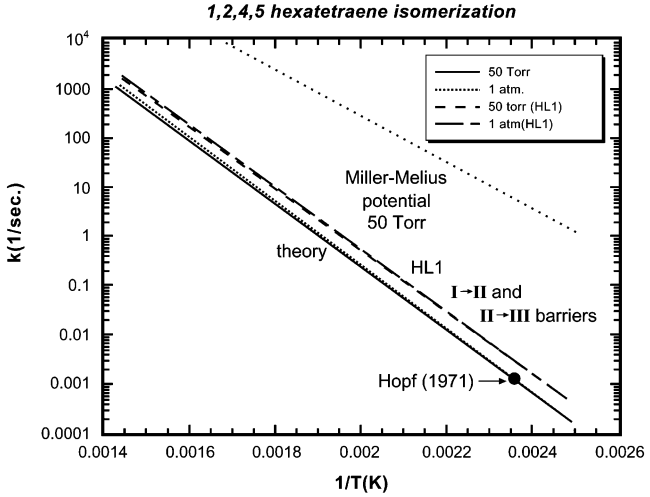

Figure 7. Arrhenius plot of the II → III rate coefficient.

a I → II barrier height that is several kcal/mol too small, a flaw in the potential that was anticipated in our previous article.[10]

Hopf[46] determined a half-life of 10 min at 424 K for 1,2,4,5-hexatetraene isomerization to 1,2-dimethylenecyclobutene, i.e., II → III, at pressures between 35 and 60 Torr. This converts to a rate coefficient of 1.16×10^{-3} s^{-1}. Figure 7 shows our predictions for the II → III rate coefficient. Hopf's experimental result is also shown on the plot. The agreement between theory and experiment is virtually perfect, a consequence of the barrier-height adjustment mentioned above. However, the unaltered HL1 barriers yield rate coefficients that are only a factor of 2 or so too high. By contrast the Miller−Melius potential in this case gives rate coefficients that are too large by 3−4 orders of magnitude, again a result of a barrier height (II → III) that is much too small.

Stein and co-workers also determined from their data a rate coefficient of $10^{12.9}$ exp($-50000/RT$) s^{-1} for isomerization of 1,2-dimethylenecyclobutene to fulvene and benzene between 733 and 823 K. Our analysis indicates that this process is not a single elementary reaction. Rather, it occurs as a result of a series of parallel and sequential steps, as one might have guessed from the potential energy surface of Figure 2. However, the process is governed by a single eigenpair of **G**, whose eigenvalue can be compared directly with Stein's "rate coefficient". This comparison is made in Figure 8. The agreement is excellent, generally within 10−20%. In this case the Miller−Melius potential yields a result that is only a factor of 3 too large.

The key flaw in the Miller−Melius potential is illustrated in Figure 9, where we have plotted the theoretical product distributions for the conditions of the Stein et al. experiments up to a temperature of 1100 K. The present potential correctly predicts the simultaneous rise of fulvene and benzene between 700 and 800 K (Figure 5); the Miller−Melius potential predicts that only fulvene is formed in this temperature range. Calculations for both potentials show conversion of fulvene to benzene for $T > 950$ K. The simultaneous formation of fulvene and benzene between 700 and 800 K requires parallel paths to these species from the early wells (I, II, and III) of the potential. In Figure 2 this path is II → VIII → ... → VII (benzene), which competes with the II → IV path and allows simultaneous formation of benzene and fulvene under the conditions of the Stein et al. experiments. On the Miller−Melius potential the only accessible path to benzene from 1,5-hexadiyne is through fulvene.

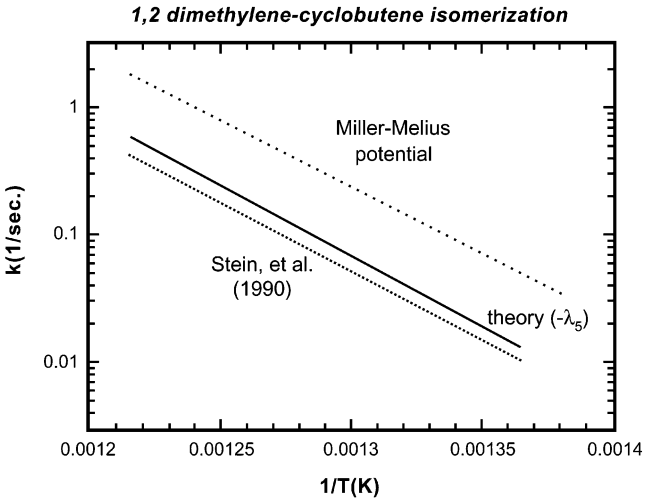

Figure 8. Arrhenius plot of the III → products "rate coefficient". As noted in the text, this is not truly an elementary reaction, but its rate is governed by a single eigenpair of G.

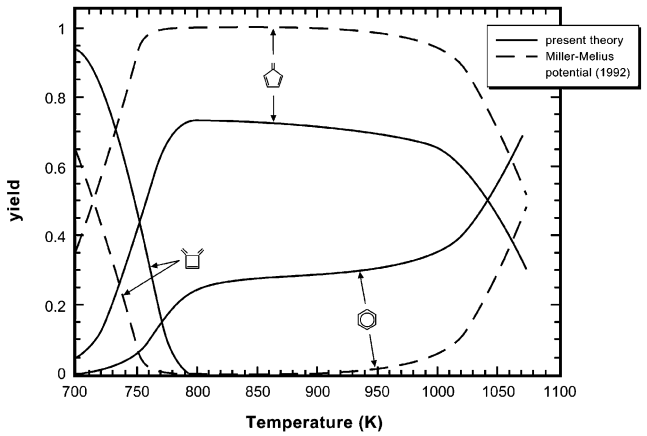

Figure 9. Product yields in the pyrolysis of 1,5-hexadiyne as a function of temperature at $p = 1$ atm. Residence time = 30 s. Similar to Figure 5, but with an expanded temperature scale to illustrate the differences between the predictions of the Miller−Melius potential and the present one.

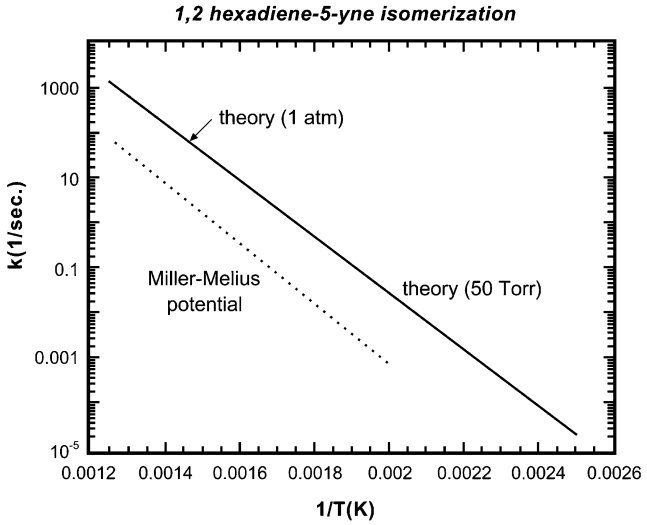

Figure 10. Arrhenius plot of the V → VI rate coefficient. Note that the 50 Torr and 1 atm theoretical curves are indistinguishable.

Figure 10 shows our theoretical prediction of the rate coefficient for isomerization of 1,2-hexadien-5-yne to 2-ethynyl-1,3-butadiene (V → VI). Hopf[47] has studied this reaction

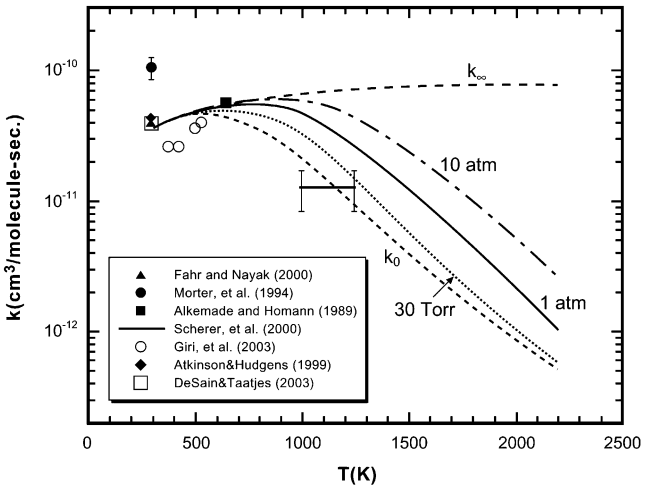

Figure 11. Total rate coefficient for the reaction $C_3H_3 + C_3H_3 \rightarrow$ products as a function of temperature and pressure.

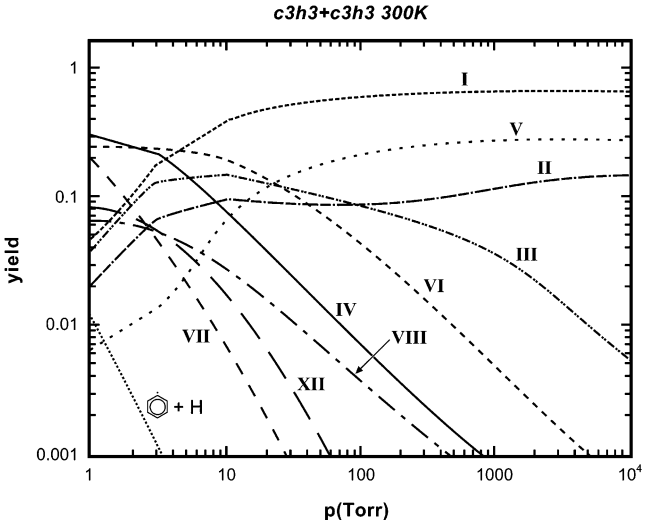

Figure 12. Product distribution for $C_3H_3 + C_3H_3 \rightarrow$ products as a function of pressure at $T = 300$ K.

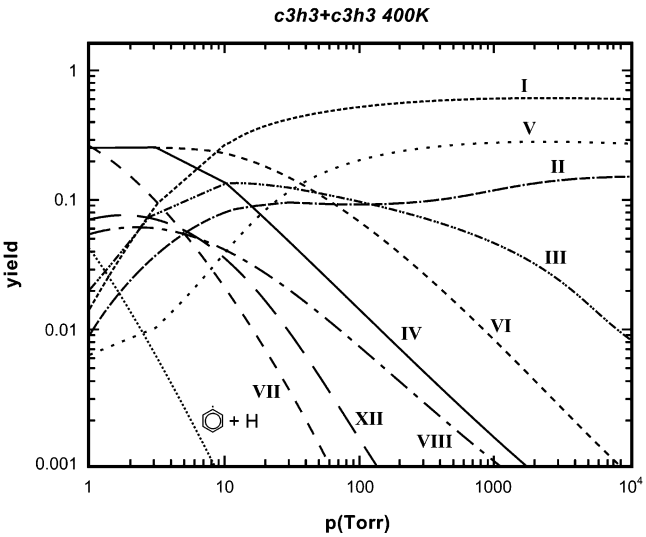

Figure 13. Product distribution for $C_3H_3 + C_3H_3 \rightarrow$ products as a function of pressure at $T = 400$ K.

experimentally between 523 and 773K. However, he does not provide any quantitative information about the rate of the reaction, indicating only that the sole product is indeed 2-ethynyl-1,3-butadiene. Our calculations confirm this conclu-

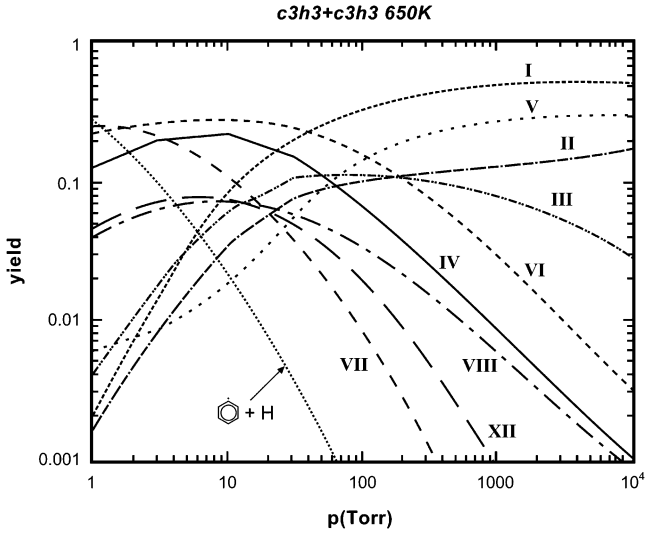

Figure 14. Product distribution for $C_3H_3 + C_3H_3 \rightarrow$ products as a function of pressure at $T = 650$ K.

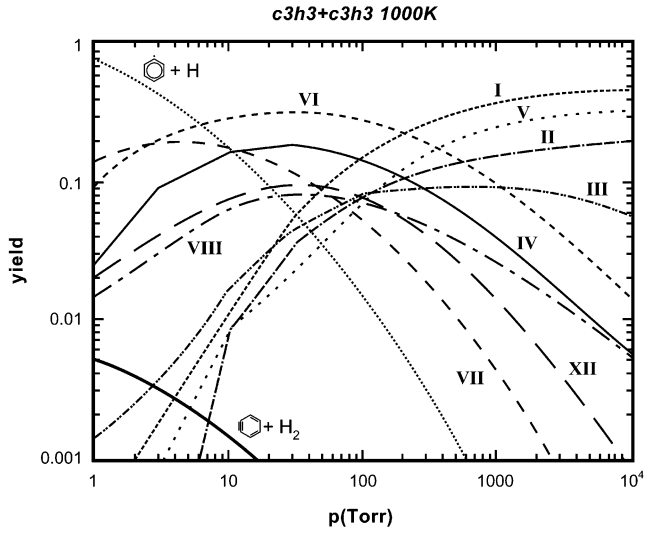

Figure 15. Product distribution for $C_3H_3 + C_3H_3 \rightarrow$ products as a function of pressure at $T = 1000$ K.

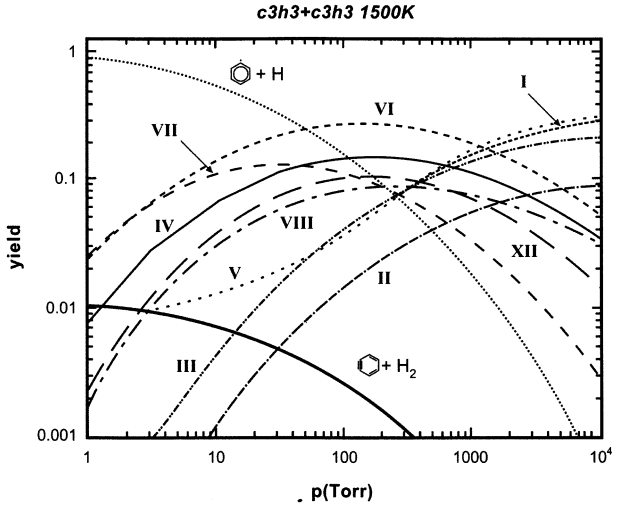

Figure 16. Product distribution for $C_3H_3 + C_3H_3 \rightarrow$ products as a function of pressure at $T = 1500$ K.

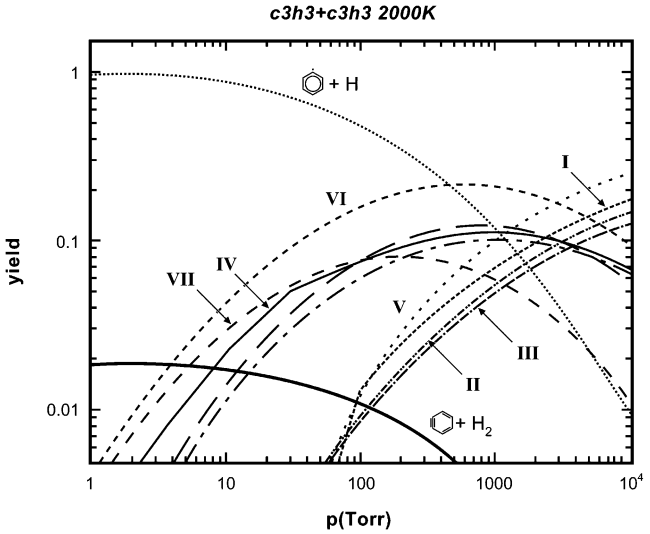

Figure 17. Product distribution for $C_3H_3 + C_3H_3 \rightarrow$ products as a function of pressure at $T = 2000$ K.

sion. We give the rate-coefficient results for possible future comparisons with experiment. The agreement between theory and experiment concerning the product at least indicates that our potential has not artificially introduced any competing paths. For this reaction, the Miller−Melius potential yields a rate coefficient that is about an order of magnitude smaller than the present result, with the same product.

An important point to note from the comparisons between theory and experiment discussed in the preceding paragraphs is that all the rate coefficients have reached their high-pressure limits under the conditions for which the comparisons are made. This limit is clearly indicated in Figures 7 and 10, where the 50 Torr and 1 atm rate coefficients are virtually identical; it is true in the other cases as well. This means that the agreement between theory and experiment does not hinge on the choice of $P(E,E')$. Thus the comparisons are about as close as one can get to being a direct test of the potential energy surface.

V. The Recombination of Propargyl Radicals

Figure 11 displays our theoretical predictions of the total rate coefficient for the $C_3H_3 + C_3H_3$ reaction as a function of temperature and pressure. As described in our previous work,[10] we have adjusted the "tightening parameters" in the "transitional potential" that describes the approach of the two propargyl radicals toward each other to predict correctly the room-temperature rate coefficient and product distribution measured by Fahr and Nayak.[48] The rate coefficient predictions in Figure 11 are similar in character to those we obtained previously. Up to $T \approx 500$ K, the total rate coefficient $k(T,p)$ is independent of pressure and equal to the capture rate coefficient k_∞(T), i.e., the high-pressure limit. For $T > 500$ K, the rate coefficient depends on pressure; for any reasonable pressure, $k(T,p)$ first increases slightly because of the temperature dependence of $k_\infty(T)$ and then drops off rapidly at high temperature. A major difference in the predictions of this work and those given previously[10] is that the present rate coefficients are considerably larger at high temperature, primarily a consequence of differences in the potential. For example, at $p = 1$ atm and $T = 1500$ K the rate coefficient of Figure 11 is almost an order of magnitude larger than that calculated from the Miller−Melius potential; the zero-pressure (or collisionless) limit rate coefficient $k_0(T)$ is roughly a factor of 4 larger in the present work. These differences are primarily due to the additional II $\rightarrow$ VIII $\rightarrow$ ... $\rightarrow$ VII $\rightarrow$ phenyl + H path on the present potential, which

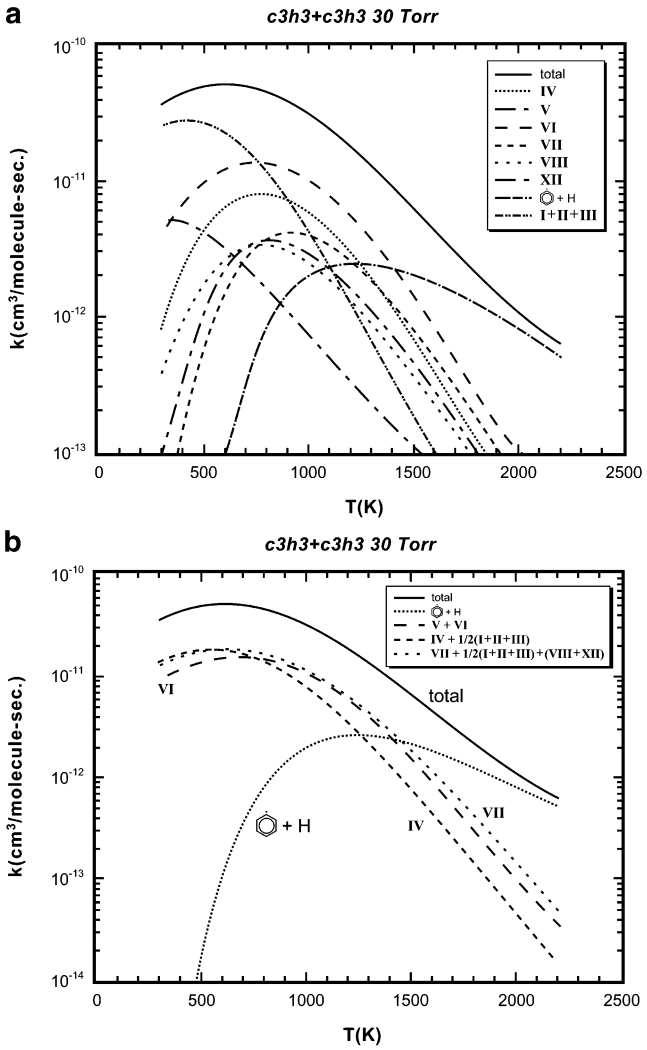

Figure 18. Lumping of product channels in the $C_3H_3 + C_3H_3$ reaction at 30 Torr: (a) rate coefficients prior to lumping; (b) rate coefficients after lumping.

bypasses the very tight IV → VII transition state and provides additional wells for stabilization.

The agreement between theory and experiment shown in Figure 11 is very good. However, the larger high-temperature rate coefficients in the present work have introduced a discrepancy between the theory and the shock-tube experiments for Scherer et al.[49] (1.5 atm $\leq p \leq$ 2.2 atm). A point in our favor is that preliminary experiments in Hippler's laboratory[50] at $p = 1$ atm are in good agreement with the present theory up to $T \approx 1500$ K. Clearly, more high-temperature measurements of the rate coefficient are desirable.

The values of $k_0(T)$, the collisionless limit rate coefficient, plotted in Figure 11 were calculated using the two-dimensional (E and J) method mentioned above. One-dimensional calculations (in E) give rate coefficients that are only a few percent larger. As before, angular momentum conservation is not a very important factor in predicting $k_0(T)$ for this reaction.

Equally as important as the total rate coefficient are the direct product distributions of the $C_3H_3 + C_3H_3$ reaction. Figures 12 through 17 show the product yields as a function of pressure for a series of temperatures between 300 and 2000 K. These plots are included here primarily to facilitate comparisons with experiment in the future. In general, high pressures and low temperatures favor the early wells along the reaction path (I,

TABLE 2: Comparison with Alkemade and Homann's Experiment

	$T = 623$ K $p = 2.25$ Torr	Alkemade/ Homann		$T = 623$ K $p = 4.5$ Torr	Alkemade/ Homann
P1	0.115		P1	0.0518	
I	0.0112	0.02	I	0.0344	0.11
II	0.00653	0.19	II	0.0170	0.09
III	0.0150		III	0.0348	
IV	0.198		IV	0.230	
V	0.00779	0.30	V	0.0104	0.46
VI	0.268		VI	0.280	
VII	0.245	0.30	VII	0.184	0.19
VIII	0.062		VIII	0.0743	
XII	0.0712		XII	0.0824	
VIII + XII	0.133	0.19	VIII + XII	0.157	0.15
	$T = 673$ K $p = 2.25$ Torr	Alkemade/ Homann		$T = 673$ K $p = 4.5$ Torr	Alkemade/ Homann
P1	0.154		P1	0.0751	
I	0.00795	0.03	I	0.0251	
II	0.00489	0.07	II	0.0130	
III	0.0114		III	0.0269	
IV	0.178		IV	0.216	
V	0.00756	0.41	V	0.00998	
VI	0.263		VI	0.282	
VII	0.247	0.30	VII	0.199	
VIII	0.0577		VIII	0.0719	
XII	0.0669		XII	0.0807	
VIII + XII	0.124	0.19	VIII + XII	0.152	

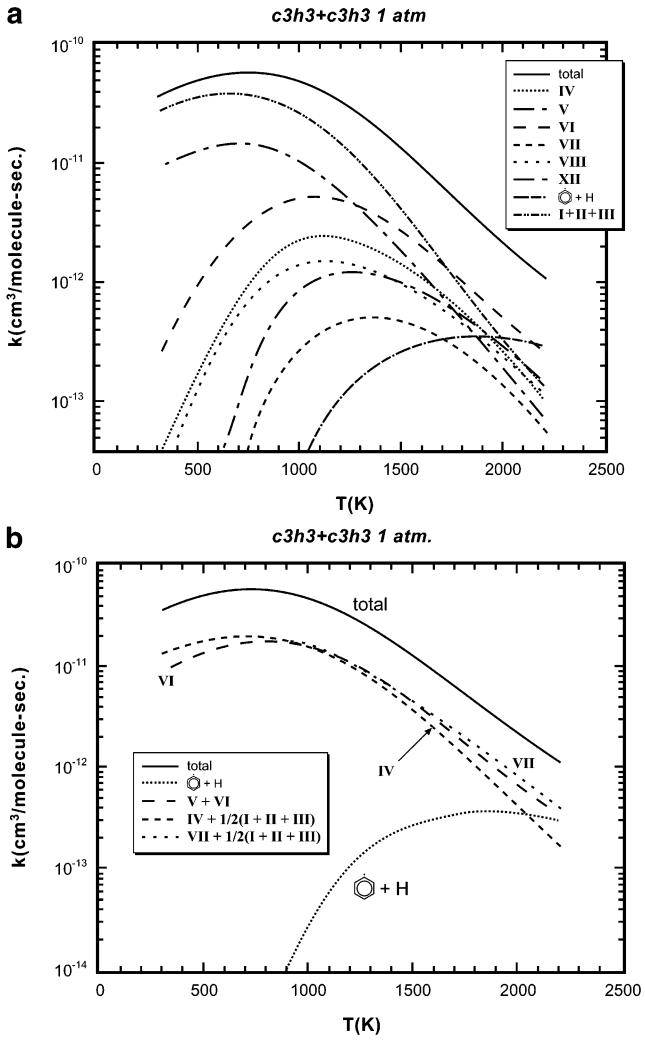

Figure 19. Lumping of product channels in the $C_3H_3 + C_3H_3$ reaction at $p = 1$ atm: (a) rate coefficients before lumping; (b) rate coefficients after lumping.

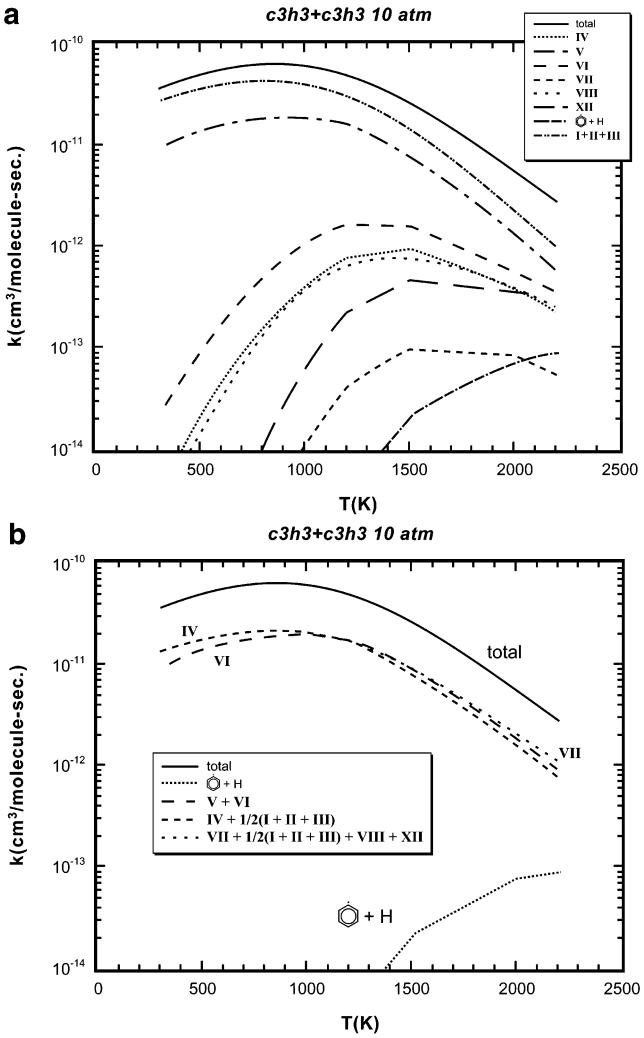

Figure 20. Lumping of product channels in the $C_3H_3 + C_3H_3$ reaction at $p = 10$ atm: (a) rate coefficients before lumping; (b) rate coefficients after lumping.

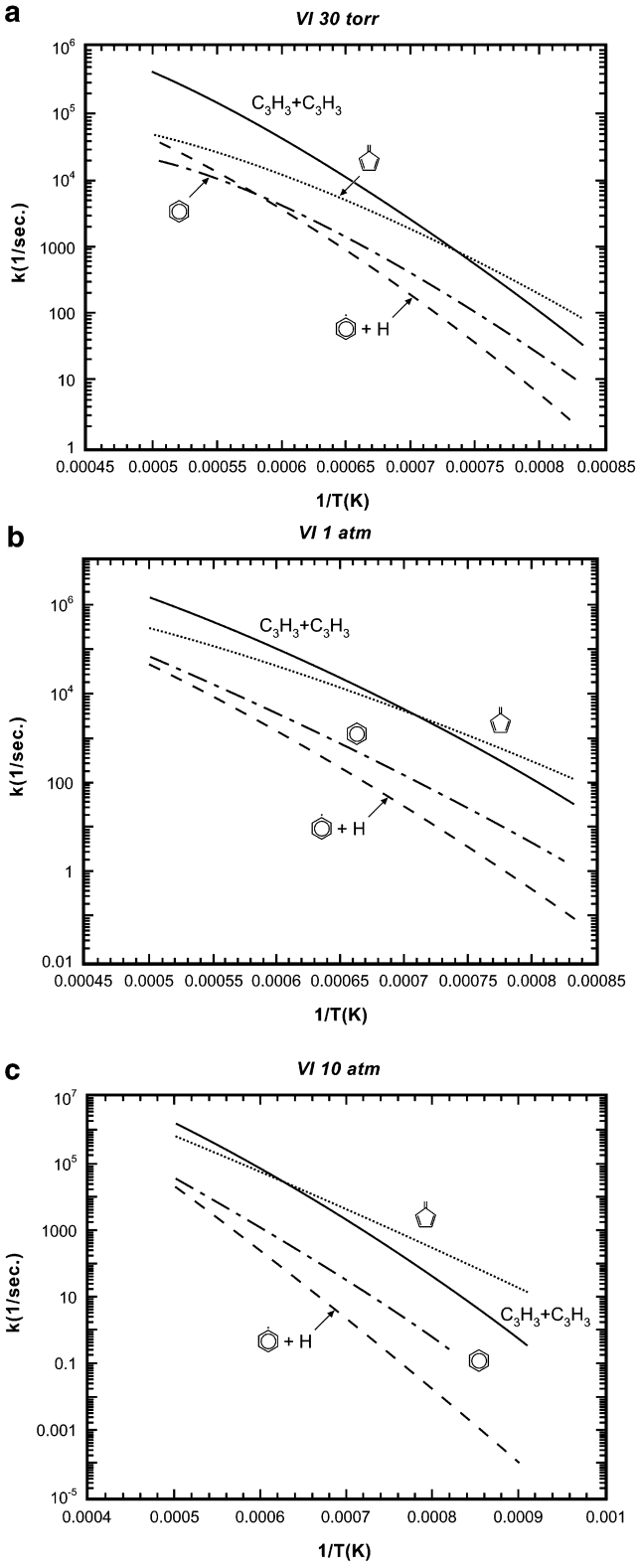

Figure 21. Rate coefficient for reactions of 2-ethynyl-1,3-butadiene (well VI): (a) $p = 30$ Torr; (b) $p = 1$ atm; (c) $p = 10$ atm.

II, V, and to some extent III), whereas high temperatures and low pressures favor phenyl + H and the C_6H_6 isomers with the longest lifetimes (VII, VI, and IV); these are typically the ones with the deepest wells. *o*-Benzyne + H_2 is never really a very important product. A good rule of thumb is that its yield is about 2 orders of magnitude smaller than that of phenyl + H. Between the high-*p*/low-*T* and low-*p*/high-*T* limits the yields are very complicated and depend on a large number of factors that we will not discuss here.

Although other experiments are currently in progress,[51−53] we are aware of only two experimental investigations in the literature of the products of the $C_3H_3 + C_3H_3$ reaction. Fahr and Nayak[48] determined the products at 295 K and 50 Torr to be 1,5-hexadiyne (∼60%), 1,2-hexadien-5-yne (∼25%), and a third, unidentified C_6H_6 isomer (∼15%). Our predictions for these conditions are 55% 1,5-hexadiyne and 18% 1,2-hexadien-5-yne, with the remainder distributed mainly among 1,2-dimethylenecyclobutene (9.5%), 1,2,4,5-hexatetraene (8%), and 2-ethynyl-1,3-butadiene (7%). Although we tailored the $C_3H_3 + C_3H_3$ approach potential to give the experimental yields at the high-pressure limit (with 1,2,4,5-hexatetraene being the third isomer), as discussed above and in our previous article,[10] there is no guarantee that we will get those results at 50 Torr. In fact, our calculations with the Miller−Melius potential gave much smaller yields of 1,5-hexadiyne for the Fahr−Nayak conditions because of the small I → II barrier height. The smaller barrier allows C_6H_6* complexes to isomerize readily from well I to well II, and on to well III. The higher I → II barrier in the present investigation gives better agreement with experiment.

Alkemade and Homann[13] have studied the $C_3H_3 + C_3H_3$ product yields at 623 and 673 K and at pressures of 2.25 and 4.5 Torr. Table 2 compares our results for these conditions with those of Alkemade and Homann. The agreement between theory

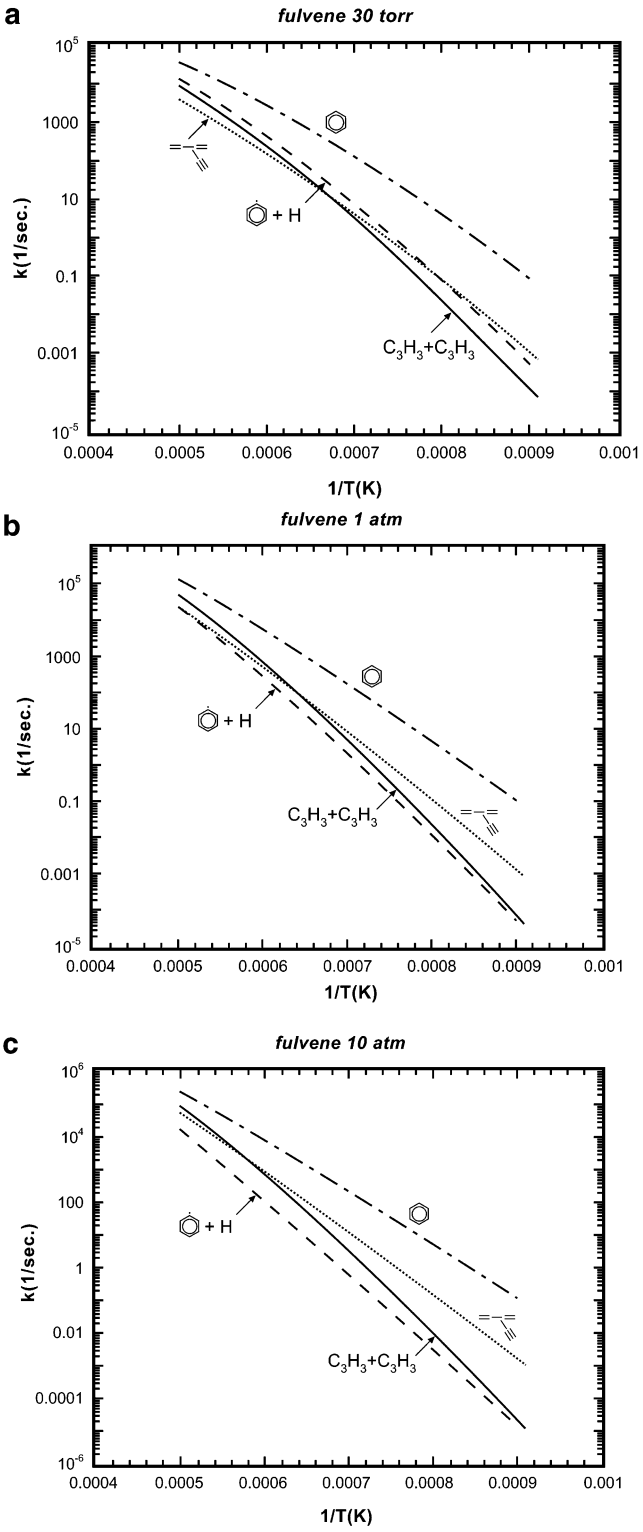

Figure 22. Rate coefficients for reactions of fulvene (well IV): (a) p = 30 Torr; (b) p = 1 atm; (c) p = 10 atm.

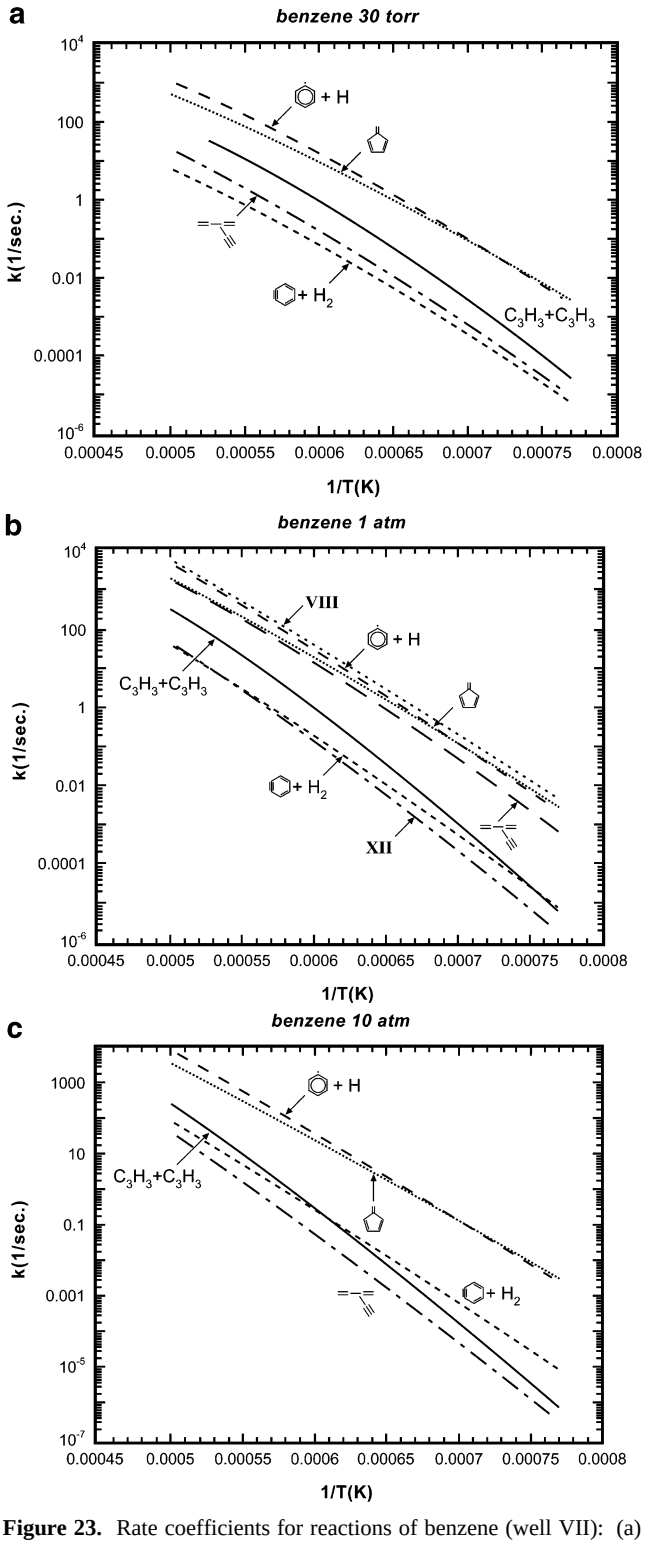

Figure 23. Rate coefficients for reactions of benzene (well VII): (a) p = 30 Torr; (b) p = 1 atm; (c) p = 10 atm. Note that, although reactions such as VII → VIII may be very fast, it is virtually impossible to detect them directly, because equilibrium heavily favors benzene at all temperatures and pressures.

and experiment is good for benzene and 1,3-hexadien-5-yne (note that wells VIII and XII are two different rotamers of 1,3-hexadien-5-yne), but it is not so good for the other species. The ME calculations indicate that, at such low pressures, C_6H_6* complexes tend to spread out over the entire potential and ultimately stabilize into the deepest wells or dissociate to phenyl + H. Under such conditions it is difficult to understand why Alkemade and Homann did not detect any fulvene, 2-ethynyl-1,3 butadiene, or phenyl + H in their experiments. Rather, the experiments favor the early wells over the later ones, particularly V over VI, to which V* complexes can isomerize readily.

The appearance of 1,3-hexadien-5-yne as an important product in both the ME predictions and the Alkemade−Homann experiments is further support for the importance of the II → VIII → ... → VII → phenyl + H path in the propargyl recombination. Wells VIII and XII are completely inaccessible on the Miller−Melius potential, as discussed in our previous

TABLE 3: Modified Arrhenius Functions for Rate Coefficients of Reactions in the Contracted Model $k(T,p) = AT^n \exp(-E_0/RT)$

reaction	$\log_{10} A$	n	E_0	temp range, K
	$p = 30$ Torr			
$C_3H_3 + C_3H_3 \rightarrow$ VI + V	48.14	−17.58	29253	300−2200
	17.16	−9.173	7568	
$C_3H_3 + C_3H_3 \rightarrow$ IV + $^1/_2$(I + II + III)	45.59	−17.02	25864	300−2200
	20.46	−10.31	7992	
$C_3H_3 + C_3H_3 \rightarrow$ VII + VIII + XII + $^1/_2$(I + II + III)	45.33	−16.73	27864	300−2200
	16.07	−8.819	7049	
$C_3H_3 + C_3H_3 \rightarrow$ phenyl + H	30.42	−11.94	28973	400−2200
	10.36	−6.722	13799	
VI → fulvene	76.76	−18.67	95531	1200−2000
VI → benzene	98.83	−24.58	122310	1200−2000
VI → phenyl + H	84.43	−20.14	121900	1200−2000
fulvene → benzene	81.75	−19.36	121500	1100−2000
fulvene → phenyl + H	97.41	−23.16	153470	1100−2000
benzene → phenyl + H	108.13	−25.81	181750	1300−2000
	$p = 1$ atm			
$C_3H_3 + C_3H_3 \rightarrow$ VI + V	36.02	−13.80	24953	300−2200
	8.627	−6.352	5432	
$C_3H_3 + C_3H_3 \rightarrow$ IV + $^1/_2$(I + II + III)	38.96	−14.73	25602	300−2200
	11.70	−7.37	5963	
$C_3H_3 + C_3H_3 \rightarrow$ VII + VIII + XII + $^1/_2$(I + II + III)	31.72	−12.55	22264	900−2200
$C_3H_3 + C_3H_3 \rightarrow$ phenyl + H	24.45	−9.977	36755	900−2200
VI → fulvene	56.37	−12.55	86405	1200−2000
VI → benzene	53.21	−11.34	100210	1200−2000
VI → phenyl + H	77.62	−17.68	133520	1200−2000
fulvene → benzene	45.16	−8.90	96999	1100−2000
fulvene → phenyl + H	68.35	−14.65	142570	1100−2000
benzene → phenyl + H	60.80	−12.40	148070	1300−2000
	$p = 10$ atm			
$C_3H_3 + C_3H_3 \rightarrow$ VI + V	37.25	−13.96	28084	300−2000
	4.726	−5.043	4517	
$C_3H_3 + C_3H_3 \rightarrow$ IV + $^1/_2$(I + II + III)	36.97	−13.93	27093	300−2000
	6.122	−5.50	4665	
$C_3H_3 + C_3H_3 \rightarrow$ VII + VIII + XII + $^1/_2$(I + II + III)	26.81	−11.01	20320	800−2000
$C_3H_3 + C_3H_3 \rightarrow$ phenyl + H	2.785	−3.879	28963	800−2000
VI → fulvene	26.69	−4.144	65424	1100−2000
VI → benzene	51.45	−10.68	106950	1200−2000
VI → phenyl + H	43.49	−7.928	118650	1200−2000
fulvene → benzene	31.47	−4.97	88465	1100−2000
fulvene → phenyl + H	24.93	−2.505	113330	1100−2000
benzene → phenyl + H	38.74	−6.178	132000	1100−2000

[a] Units of A are cm^3, molecules, K and seconds with the moleclarity of the reaction was written. Where two sets of modified Arrhenius parameters are given, the correct rate coefficient is the sum of the two. R = 1.987 cal/(mol K).

article. This failure to predict a significant experimental product was a factor in motivating our search for the new path.

It should be clear that the discrepancies between the present theory and the Alkemade−Homann experiments are not likely to be the fault of the potential. As discussed above, the low-temperature isomerization experiments are a fairly direct test of the most important features of the PES, and they tend to confirm the present model. Most likely the model of the $P_i(E,E')$ function used in the ME calculations is to blame, at least to some extent. However, improving this model would require tailoring the "well dependence" of $P_i(E,E')$ to increase stabilization into the early wells without substantially affecting the benzene and 1,3-hexadien-5-yne predictions. At the present time there is no independent guidance as to how to do this. Consequently, it seems prudent to forego this exercise, at least until more experimental results become available.

There is one last experimental test that we can apply to our theoretical predictions. Scherer et al.[49] give an upper limit on the rate coefficient for formation of phenyl + H of 8.3×10^{-13} cm^3/(molecule s) for 1400 K < T < 1600 K at pressures around 1−2 atm. Our largest rate coefficient for this channel under such conditions is approximately 3×10^{-13} cm^3/(molecule s), well below this upper limit.

VI. An Approximate Model for the Kinetics of C_3H_3 + C_3H_3 Recombination

Our knowledge of the product distributions in the propargyl + propargyl recombination does not warrant extracting all 104 forward rate coefficients mentioned above from the master equation analysis, at least at the present time. Instead, we propose a much simpler description of the chemistry to be used in combustion modeling. Master equation calculations at combustion temperatures (∼1500 K) indicate that, on time scales of no more than several microseconds, the vast majority of the C_6H_6 isomers react, after being formed from $C_3H_3 + C_3H_3$, and are ultimately stabilized as either benzene, fulvene, or 2-ethynyl-1,3-butadiene, or they may dissociate to phenyl + H (or perhaps $C_3H_3 + C_3H_3$). Such a conclusion might also be drawn from examining Figure 4 carefully, where virtually all the chemical eigenmodes, except those involving the species mentioned above, relax on a microsecond time scale, or faster. The exception to this rule is the two rotamers of 1,3-hexadien-5-yne (wells VIII and XII), which tend to live somewhat longer, but they are never major products of the $C_3H_3 + C_3H_3$ reaction anyway. Consequently, we propose a simplified model of the $C_3H_3 + C_3H_3$ recombination in which all the products are

lumped into the four different product channels mentioned above. Master equation calculations indicate that the following lumpings are appropriate for such a contracted description of the chemistry (the species to the left and right of the arrows, respectively, indicate before and after lumping):

$$\text{IV} + {}^1/_2(\text{I} + \text{II} + \text{III}) \rightarrow \text{fulvene (IV)}$$

$$\text{V} + \text{VI} \rightarrow \text{2-ethynyl-1,3-butadiene (VI)}$$

$$\text{VII} + {}^1/_2(\text{I} + \text{II} + \text{III}) + \text{VIII} + \text{XII} \rightarrow \text{benzene(VII)}$$

$$\text{phenyl} + \text{H} \rightarrow \text{phenyl} + \text{H}$$

Such a model is fatally flawed if pushed too hard, particularly at high pressure and low temperature, but it represents a reasonable compromise between a "complete" description of the chemistry and one in which everything is lumped into benzene or phenyl + H, as has normally been done in the past. Figures 18−20 show the ME rate coefficients and the lumped ones for the three pressures: 30 Torr, 1 atm, and 10 atm.

In addition to the $C_3H_3 + C_3H_3$ rate coefficient, isomerization/dissociation rate coefficients involving the major products are required for our model. The necessary rate coefficients are given in Figures 21 (2-ethynyl-1,3-butadiene), 22 (fulvene), and 23 (benzene) for the three pressures, along with a few rate coefficients that are not required for the model. There is remarkably little experimental work with which to compare our predictions for these rate coefficients. Only the fulvene → benzene (IV → VII) rate coefficient has been measured in the laboratory, and it has been measured only once, by Gaynor et al.,[54] using very low-pressure pyrolysis in the temperature range 1050 K < T < 1150 K. Our predictions at the high-pressure limit are about a factor of 5 smaller than their determination. Madden et al.[55] have also tried to predict the Gaynor et al. result, and their rate coefficient is a factor of 2 smaller than ours. We could obtain agreement with the experiment by adjusting the IV → VII (i.e., B → IX of Figure 2) barrier height downward. However, it seems premature to make such a modification to the potential at this point.

Table 3 gives modified Arrhenius expressions (or sums of modified Arrhenius expressions) for all the rate coefficients required by the model at pressures of 30 Torr, 1 atm, and 10 atm.

VII. Concluding Remarks

We have investigated in some detail the rate coefficient and product distribution of the reaction between two propargyl radicals. This work has involved new characterizations of important stationary points on the C_6H_6 potential and utilizes methods we have described previously[8,9] for determining phenomenological rate coefficients from an RRKM-based, multiple-well master equation. The most important feature of the new potential (over the Miller−Melius potential we used previously) is the II → VIII → ... → VII → phenyl + H path shown in Figure 2. This path allows us to predict correctly the simultaneous formation of fulvene and benzene in the experiments of Stein et al.[12] on the pyrolysis of 1,5-hexadiyne. It also allows us to predict correctly the appearance of 1,3-hexadien-5-yne as a significant product in the $C_3H_3 + C_3H_3$ recombination experiments of Alkemade and Homann.[13]

Overall, the agreement of our theoretical predictions with experiment is good, but not excellent. In fact, there is very little experimental data with which to compare. In this spirit, we have proposed an approximate model for the kinetics of the $C_3H_3 + C_3H_3$ recombination (and subsequent isomerizations and dissociations) for use in flame modeling. In this contracted model only the most stable products are included explicitly, namely, phenyl + H, benzene, fulvene, and 2-ethynyl-1,3-butadiene. The thermal rate coefficients required for the model are given in modified Arrhenius form.

Acknowledgment. This work was supported by the United States Department of Energy, Office of Basic Energy Sciences, Division of Chemical Sciences, Geosciences, and Biosciences. Sandia is a multiprogram laboratory operated by Sandia Corp., a Lockheed Martin Co., for the United State Department of Energy under contract DE-AC04-94-AL85000.

Supporting Information Available: Cartesian coordinates and vibrational frequencies of the structures in Figure 3. This material is available free of charge via the Internet at http://pubs.acs.org.

References and Notes

(1) Miller, J. A. *Proc. Combust. Inst.* **1996**, *26*, 461−480.
(2) Miller, J. A. *Faraday Discuss.* **2001**, *119*, 461−475.
(3) Miller, J. A.; Melius, C. F. *Combust. Flame* **1992**, *91*, 21.
(4) Richter, H.; Howard, J. B. *Prog. Energy Combust. Sci.* **2000**, *26*, 565−608.
(5) Miller, J. A.; Kee, R. J.; Westbrook, C. K. *Annu. Rev. Phys. Chem.* **1990**, *41*, 345−387.
(6) Lindstedt, P. *Proc. Combust. Inst.* **1998**, *27*, 269−285.
(7) Wu, C. J.; Kern, R. D. *J. Phys. Chem.* **1987**, *91*, 6291−6296.
(8) Klippenstein, S. J.; Miller, J. A. *J. Phys. Chem. A* **2002**, *106*, 9267−9277.
(9) Miller, J. A.; Klippenstein, S. J. *J. Phys. Chem. A* **2003**, *107*, 2680−2692.
(10) Miller, J. A.; Klippenstein, S. J. *J. Phys. Chem. A* **2001**, *105*, 7254−7266.
(11) Melius, C. F.; Miller, J. A.; Evleth, E. M. *Proc. Combust. Inst.* **1992**, *24*, 621−628.
(12) Stein, S. E.; Walker, J. A., Suryan, M. M.; Fahr, A. *Proc. Combust. Inst.* **1990**, *23*, 85−90.
(13) Alkemade, U.; Homann, K. H. *Z. Phys. Chem. Neue Folge* **1989**, *161*, 19−34.
(14) Becke, A. D. *J. Chem. Phys.* **1993**, *98*, 5648.
(15) Hehre, W. J.; Radom, L.; Pople, J. A.; Schleyer, P. v. R. *Ab Initio Molecular Orbital Theory*; Wiley: New York, 1987.
(16) Curtiss, L. A.; Raghavachari, K.; Redfern, P. C.; Rassolov, V.; Pople, J. A. *J. Chem. Phys.* **1998**, *109*, 7764.
(17) Martin, J. M. L. *Chem. Phys. Lett.* **1996**, *259*, 669.
(18) Feller, D.; Dixon, D. A. *J. Chem. Phys.* **2001**, *115*, 3484−3496.
(19) Dunning, T. H. *J. Chem. Phys.* **1989**, *90*, 1007.
(20) Frisch, M. J.; Trucks, G. W.; Schlegel, H. B.; Scuseria, G. E.; Robb, M. A.; Cheeseman, J. R.; Zakrzewski, V. G.; Montgomery, J. A., Jr.; Stratmann, R. E.; Burant, J. C.; Dapprich, S.; Millam, J. M.; Daniels, A. D.; Kudin, K. N.; Strain, M. C.; Farkas, O.; Tomasi, J.; Barone, V.; Cossi, M.; Cammi, R.; Mennucci, B.; Pomelli, C.; Adamo, C.; Clifford, S.; Ochterski, J.; Petersson, G. A.; Ayala, P. Y.; Cui, Q.; Morokuma, K.; Malick, D. K.; Rabuck, A. D.; Raghavachari, K.; Foresman, J. B.; Cioslowski, J.; Ortiz, J. V.; Stefanov, B. B.; Liu, G.; Liashenko, A.; Piskorz, P.; Komaromi, I.; Gomperts, R.; Martin, R. L.; Fox, D. J.; Keith, T.; Al-Laham, M. A.; Peng, C. Y.; Nanayakkara, A.; Gonzalez, C.; Challacombe, M.; Gill, P. M. W.; Johnson, B.; Chen, W.; Wong, M. W.; Andres, J. L.; Gonzalez, C.; Head-Gordon, M.; Replogle, E. S.; Pople, J. A. *Gaussian98*; Gaussian, Inc.: Pittsburgh, PA, 1998.
(21) Klippenstein, S. J. Unpublished results.
(22) Klippenstein, S. J. *J. Phys. Chem.* **1992**, *96*, 367−372.
(23) Klippenstein, S. J. *J. Phys. Chem.* **1994**, *98*, 11459−11464.
(24) Harding, L. B.; Klippenstein, S. J. *Phys. Chem. Chem. Phys.* **1999**, *1*, 989−997.
(25) Muller-Markgraf, W.; Troe, J. *J. Phys. Chem.* **1998**, *92*, 4914.
(26) Ackermann, L.; Hippler, H.; Pagsberg, P.; Reihs, C.; Troe, J. *J. Phys. Chem.* **1990**, *94*, 5247.
(27) Braun-Unkhoff, M.; Frank, P.; Just, Th. *Proc. Combust. Inst.* **1989**, *22*, 1053.
(28) Mebel, A. M.; Lin. S. H.; Yang, X. M.; Lee, Y. T. *J. Phys. Chem. A* **1997**, *101*, 6781−6789.
(29) Madden, L. K.; Mebel, A. M.; Lin, M. C.; Melius, C. F. *J. Phys. Org. Chem.* **1996**, *9*, 801−810.

(30) Mebel, A. M.; Lin, M. C.; Chakraborty, D.; Park, J.; Lin, S. H.; Lee, Y. T. *J. Chem. Phys.* **2001**, *114*, 8421−8435.
(31) Bettinger, H. F.; Schreiner, P. R.; Schaefer, H. F.; Schleyer, P. v. R. *J. Am. Chem. Soc.* **1998**, *120*, 5741−5750.
(32) Miller, J. A.; Klippenstein, S. J. *J. Phys. Chem. A* **2000**, *104*, 2061−2069.
(33) Miller, J. A.; Klippenstein, S. J.; Robertson, S. H. *J. Phys. Chem. A* **2000**, *104*, 7525−7536 and 9806 (correction).
(34) Miller, J. A.; Klippenstein, S. J.; Robertson, S. H. *Proc. Combust. Inst.* **2000**, *28*, 1479.
(35) Miller, J. A.; Klippenstein, S. J. *Int. J. Chem. Kinet.* **2001**, *3*, 654−668.
(36) Hahn, D. K.; Klippenstein, S. J.; Miller, J. A. *Faraday Discuss.* **2001**, *119*, 159.
(37) Widom, B. *Science* **1965**, *148*, 1555−1560.
(38) Widom, B. *J. Chem. Phys.* **1971**, *55*, 44−52.
(39) Widom, B. *J. Chem. Phys.* **1974**, *61*, 672−680.
(40) Bartis, J. T.; Widom, B. *J. Chem. Phys.* **1974**, *60*, 3474−3482.
(41) Miller, J. A.; Parrish, C.; Brown, N. J. *J. Phys. Chem.* **1986**, *90*, 3339.
(42) Hold, U.; Lenzer, T.; Luther, K.; Reihs, K.; Symonds, A. *Ber. Bunsen-Ges. Phys. Chem.* **1997**, *101*, 552−565.
(43) Miller, J. A.; Klippenstein, S. J.; Raffy, C. *J. Phys. Chem. A* **2002**, *106*, 4904−4913.
(44) Klippenstein, S. J.; Wagner, A. F.; Dunbar, R. C.; Wardlaw, D. M.; Robertson, S. H.; Miller, J. A. VARIFLEX Version 1.12m, 2002.
(45) Huntsman, W. D.; Wristers, H. J. *J. Am. Chem. Soc.* **1967**, *89*, 342.
(46) Hopf, H. *Chem. Ber.* **1971**, *104*, 1499−1506.
(47) Hopf, H. *Agnew. Chem.* **1970**, *82*, 703.
(48) Fahr, A.; Nayak, A. *Int. J. Chem. Kinet.* **2000**, *32*, 118−124.
(49) Scherer, S.; Just, Th.; Frank, P. *Proc. Combust. Inst.* **2000**, *28*, 1511−1518.
(50) Giri, B. R.; Hippler, H.; Olzmann, M.; Unterreiner, A. N. Poster presented at Seventeeth International Symposium on Gas Kinetics, Essen, Germany. August 24−29, 2002.
(51) Giri, B. R.; Hippler, H.; Olzmann, M.; Unterreiner, A. N. Private communication, 2002.
(52) Shafir, E. V.; Slagle, I. R.; Knyazev, V. D. Kinetics of the Self-Reactions of Propargyl Radicals, presented at the Seventeenth International Symposium of Gas Kinetics, Essen, Germany, August 24−29, 2002.
(53) Miyoshi, A. Private communication, 2003.
(54) Gaynor, B. J.; Gilbert, R. G.; King, K. D.; Harman, P. J. *Aust. J. Chem.* **1981**, *34*, 449−452.
(55) Madden, L. K.; Mebel, A. M.; Lin, M. C.; Melius, C. F. *J. Phys. Org. Chem.* **1996**, *9*, 801−810.
(56) Atkinson, D. B.; Hudgens, J. W. *J. Phys. Chem. A* **1999**, *103*, 4242−4252.
(57) Morter, C. L.; Farhat, S. K.; Adamson, J. D.; Glass, G. P.; Curl, R. F. *J. Phys. Chem.* **1994**, *98*, 7029−7035.
(58) DeSain, J. D.; Taatjes, C. A. *J. Phys. Chem. A.* **2003**, *107*, 4843−4850.